

Optimal Uncertainty Quantification under General Moment Constraints on Input Subdomains

Rong Jin^a, Xingsheng Sun^{a,*}

^aDepartment of Mechanical and Aerospace Engineering, University of Kentucky, Lexington, KY, 40506, United States

ARTICLE INFO

Keywords:

Optimal uncertainty quantification
Epistemic and aleatory uncertainties
Safety certification
Inverse transform sampling
Ballistic impact

ABSTRACT

We present an optimal uncertainty quantification (OUQ) framework for systems whose uncertain inputs are characterized by truncated moment constraints defined over subdomains. Given such partial uncertainty information, rigorous optimal upper and lower bounds on the probability of failure (PoF) can be derived over the admissible set of probability measures, providing a principled basis for system safety certification. We formulate the OUQ problem under general moment constraints on subdomains and develop a high-performance computational framework to compute the corresponding optimal bounds. The proposed approach transforms the original infinite-dimensional optimization problems, constrained by subdomain-based moment information, into finite-dimensional unconstrained optimization problems parameterized solely by free canonical moments. To address the prohibitive cost of PoF evaluation in high-dimensional settings, we further incorporate inverse transform sampling (ITS), which enables efficient and accurate estimation of the PoF within the OUQ optimization. We also examine a special case in which the uncertain inputs are constrained only by zeroth-order moments over subdomains, and demonstrate that the resulting OUQ formulation is equivalent to the evidence theory. The effectiveness and scalability of the framework are demonstrated through three groups of numerical examples involving varying numbers of subdomains and moment constraints. The results show that increasing either the number of subdomains or the order of moment constraints systematically decreases the upper bound and increases the lower bound, thereby tightening the bound interval. For high-dimensional problems, the ITS strategy reduces the computational cost by up to two orders of magnitude while maintaining a relative error below 1%. In addition, we identify regimes in which the optimal bounds are more sensitive to subdomain partitioning or to higher-order moment information. These findings provide practical guidance for prioritizing uncertainty reduction efforts when certifying system safety.

1. Introduction

Uncertainties are inherent in nearly all engineering analyses and decision-making processes, arising from diverse sources ranging from material inhomogeneity to model simplifications [1–3]. These uncertainties can significantly affect the accuracy and reliability of design predictions. Although the use of appropriately chosen safety factors can mitigate the impact of such uncertainties, the resulting designs and products may fail to achieve the desired balance between performance, efficiency, and economy. Therefore, it is essential to quantify and assess the effects of different sources of uncertainty on engineering solutions to provide decision-makers with reliable predictions and quantitative measures of confidence in these predictions.

The design process typically involves constructing a model that reproduces the behavior of the real structure under specified loading conditions. Consequently, it is relatively straightforward to represent the model's input parameters and output responses using appropriate uncertainty models. Once these uncertainties are characterized, their influence on relevant performance measures can be systematically analyzed and quantified, enabling designers to identify potential weaknesses and refine the design as necessary to enhance robustness and reliability.

Based on their nature and reducibility, uncertainties are commonly classified into aleatory (inherent variability) and epistemic (lack of knowledge) [4]. Aleatory uncertainties arise from natural randomness—such as material inhomogeneity, manufacturing tolerances, and environmental fluctuations—and are irreducible, even with improved modeling or measurement. Given sufficient data, these inherent variations can typically be characterized using a probability density function (PDF). The most straightforward approach for propagating aleatory uncertainties involves Monte Carlo-based sampling methods [5], often grounded in Bayesian inference [6]. A critical step in these approaches

*Corresponding author at: Department of Mechanical and Aerospace Engineering, University of Kentucky, Lexington, KY 40506, United States.
E-mail address: xingsheng.sun@uky.edu (X. Sun)

is the appropriate selection of PDFs for the uncertain parameters, as this choice can significantly influence the resulting predictions [7–9].

In contrast, epistemic uncertainties originate from incomplete or imperfect knowledge, including model simplifications, numerical approximations, measurement errors, and limited experimental data. Unlike aleatory uncertainties, they can often be reduced through refined models, additional data, or improved experimental techniques. Traditionally, epistemic uncertainties are represented using non-probabilistic methods. For example, evidence theory (also known as Dempster-Shafer theory) expresses uncertainty by assigning degrees of belief and plausibility to events [10, 11]. Probability boxes (p-boxes) define envelopes of possible PDFs constrained by available statistical information such as means and variances [12]. Interval analysis represents uncertain quantities as bounded ranges, with computations carried out using interval arithmetic to ensure that the true (but unknown) values are guaranteed to lie within the resulting intervals [13]. Fuzzy probability theory employs fuzzy numbers, typically characterized by membership functions, to express a continuum of possible probabilities along with their degrees of plausibility [14]. A comprehensive review of epistemic uncertainty models can be found in Ref. [15]. It is worth noting that aleatory and epistemic uncertainties are not always easily distinguishable during the characterization of input variables or the modeling and solution of engineering systems. When both types coexist and interact, they are collectively referred to as polymorphic uncertainties [16].

More recently, a distinctive approach known as Optimal Uncertainty Quantification (OUQ) has been developed to compute rigorous bounds on quantities of interest (QoIs), such as the upper and lower limits of the probability of failure (PoF) [17]. Unlike traditional methods, OUQ can incorporate partial information about input (or prior) probability measures without requiring the full specification of a PDF or other explicit uncertainty models. Specifically, OUQ reformulates the infinite-dimensional optimization problem of bounding the PoF into a finite-dimensional problem expressed as a convex combination of Dirac measures [18, 19]. By optimizing the supports and weights of these Dirac measures, OUQ yields the mathematically sharpest possible bounds on the QoI. In the OUQ framework, partial information of uncertainties—such as variable bounds, means, or higher-order moments—is incorporated as constraints in the optimization problem, ensuring that the computed bounds are both rigorous and consistent with the available knowledge. The OUQ framework has been successfully applied to a wide range of engineering problems, including the design of thermal-hydraulic reactors [20], ballistic impact analysis of aluminum and magnesium alloys [21, 22], rupture prediction of soft collagenous tissues [23], and the buckling analysis of wide-flange columns [24].

Most previous OUQ studies have focused on incorporating statistical information defined globally over the entire support of random inputs [20–26]. However, in practical applications, statistical information can also be available only within specific subdomains or subintervals of the input space [27–30]. This allows the estimation of local or subdomain-specific statistical moments, such as conditional means, variances, or higher-order moments, based on data confined to particular intervals of the random input. In other regions where data are scarce or unavailable, expert judgment or prior qualitative knowledge may provide additional information that should also be incorporated into the UQ process. In addition to experimental measurements, computational simulations can be used to estimate statistical moments—such as skewness and kurtosis—through various approaches. Examples include lower-scale statistical volume element simulations [31], sparse approximations in moment-based arbitrary polynomial chaos [32], and inverse stochastic analyses based on non-sampling generalized polynomial chaos [33], among others. Nevertheless, beyond the bounds and mean values of random variables, higher-order statistical information is often difficult to obtain due to limited data availability and computational cost. This raises the need for prior numerical investigations to identify which higher-order moments and subdomain-specific information most significantly influence the system's probabilistic response.

To address these challenges, the present study extends the OUQ framework to compute optimal bounds on the PoF in cases where partial uncertainty information is available locally only over subdomains of the input space. We aim to mathematically formulate and solve the corresponding optimization problem, and to systematically examine how the number of subdomains and the number of prescribed statistical moments affect the optimal bounds on the PoF.

The remainder of the paper is organized as follows. Section 2 formulates the OUQ problem under general truncated moment constraints and outlines the corresponding solution strategies. Section 3 examines a special case of OUQ under zeroth-order moment constraints and compares the resulting formulation with evidence theory. Section 4 presents three numerical examples, including identity functions of four basic distributions, a five-dimensional nonlinear problem, and a ballistic impact problem. Finally, Section 5 concludes the paper with a summary of key findings and a discussion of future directions.

2. Methodology

In this section, we begin with a brief overview of the OUQ framework. We then formulate the OUQ problem under general truncated moment constraints and describe its solution using reduction theorem, a canonical-moment-based approach, eigendecomposition of the Jacobi matrix, and inverse transform sampling (ITS). Readers are referred to Ref. [17] for details on the reduction theorem and to Ref. [34] for the canonical-moment methodology.

2.1. Optimal Uncertainty Quantification and Certification

In this work, we consider a system characterized by a validated physics-based model. In the context of UQ, we aim to determine the probabilities of system outcomes when the response is stochastic or uncertain due to variability or lack of knowledge in the system inputs or operating conditions. Specifically, the system performance is described by a known response function

$$Y = G(X), \quad (1)$$

where the forward mapping $G : \mathcal{X} \rightarrow \mathcal{Y}$ transforms the input space $\mathcal{X} \equiv \prod_{i=1}^m \mathcal{X}_i \subseteq \mathbb{R}^m$ into the output space $\mathcal{Y} \equiv \prod_{i=1}^n \mathcal{Y}_i \subseteq \mathbb{R}^n$. The input vector $X \equiv (X_1, \dots, X_m)$ consists of m independent random variables, where each $X_i \in \mathcal{X}_i$ ($i = 1, 2, \dots, m$), representing imperfectly known or uncertain properties of the system. The output vector $Y \equiv (Y_1, \dots, Y_n)$, with each $Y_i \in \mathcal{Y}_i$ ($i = 1, 2, \dots, n$), corresponds to the system's performance measures. The random inputs are generated according to an unknown probability law $\mathbb{P} \in \Phi(\mathcal{X})$, defined on the measurable space \mathcal{X} and possibly subject to certain known characteristics (e.g., bounds, moments).

A representative example of uncertainty quantification in engineering is design certification, which involves assessing the probability that a system will perform safely and remain within specified operational limits. The design requirements impose that the output Y must remain within an *admissible* set $\mathcal{Y}^a \subseteq \mathcal{Y}$. Failure occurs when Y falls within the *inadmissible* set $\mathcal{Y}^c = \mathcal{Y} \setminus \mathcal{Y}^a$. Ideally, the probability measure associated with Y would have its entire support contained within the admissible set, i.e.,

$$\mathbb{P}[Y \in \mathcal{Y}^a] = 1. \quad (2)$$

Systems satisfying this condition can be certified with complete certainty. However, such absolute assurance of safe performance is often impractical or unattainable, for example, when \mathbb{P} lacks compact support or when achieving it would be prohibitively costly. In practice, this strict condition is typically relaxed by introducing an acceptable PoF. Let $\epsilon \in [0, 1]$ denote the maximum tolerable PoF. The system is considered *safe* if

$$\mathbb{P}[Y \in \mathcal{Y}^c] \leq \epsilon, \quad (3)$$

and *unsafe* if

$$\mathbb{P}[Y \in \mathcal{Y}^c] > \epsilon. \quad (4)$$

However, due to incomplete information, the exact probability measure of the input random variables X is generally unknown. To address this, we define a subset

$$\mathcal{A} \subseteq \{\mu \mid \mu \in \Phi(\mathcal{X})\}, \quad (5)$$

which encodes all available information about the probability measure \mathbb{P} of X . This information may originate from experimental data, lower-fidelity simulations, or expert judgment. By construction, the true measure \mathbb{P} is assumed to belong to \mathcal{A} . Within this admissible set, some scenarios may be *safe* (i.e., $\mu[Y \in \mathcal{Y}^c] \leq \epsilon$), while others may be *unsafe* (i.e., $\mu[Y \in \mathcal{Y}^c] > \epsilon$). Given this information set \mathcal{A} , it is possible to determine *rigorous* and *optimal* upper and lower bounds on the PoF, corresponding to the most and least conservative scenarios consistent with the assumptions. These bounds are defined as

$$U(\mathcal{A}) := \sup_{\mu \in \mathcal{A}} \mu[Y \in \mathcal{Y}^c], \quad (6a)$$

$$L(\mathcal{A}) := \inf_{\mu \in \mathcal{A}} \mu[Y \in \mathcal{Y}^c]. \quad (6b)$$

The bounds $U(\mathcal{A})$ and $L(\mathcal{A})$ defined in Eq. (6) provide a rigorous basis for solving the certification problem. Assuming that the information set \mathcal{A} is valid (i.e., $\mathbb{P} \in \mathcal{A}$), the following criteria apply: if $U(\mathcal{A}) \leq \epsilon$, the system is *certifiably safe*; if $\epsilon < L(\mathcal{A})$, the system is *certifiably unsafe*; and if $L(\mathcal{A}) \leq \epsilon < U(\mathcal{A})$, the available information is insufficient to determine the system's safety. This certification logic and its optimality are illustrated in Fig. 1(a). In addition, the tightness of these bounds depends directly on the information contained in \mathcal{A} . For two information sets \mathcal{A}_1 and \mathcal{A}_2 , if $\mathcal{A}_1 \subseteq \mathcal{A}_2$, then $U(\mathcal{A}_1) \geq U(\mathcal{A}_2)$ and $L(\mathcal{A}_1) \leq L(\mathcal{A}_2)$. In other words, the more information about uncertainties is incorporated into the UQ analysis, the tighter the resulting bounds $U(\mathcal{A})$ and $L(\mathcal{A})$ become, and the closer they approach the true PoF, as shown in Fig. 1(b). This tightening improves the efficiency of certification but generally increases computational cost, which reveals a fundamental trade-off between the economy of certification and computational feasibility.

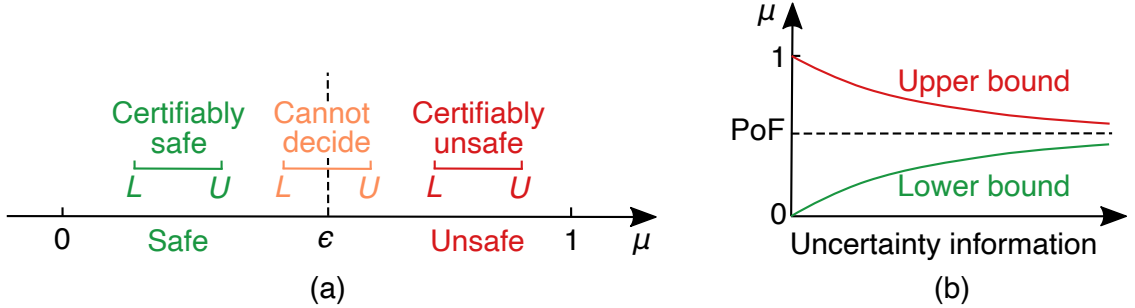


Figure 1: Illustration of certification in OUQ: (a) Rigorous decision criterion for system safety, and (b) Convergence of optimal bounds with increasing information.

2.2. OUQ under Local Moment Constraints

In this work, we consider a scenario in which the input domain of the system, \mathcal{X} , is partitioned into multiple subdomains. Without loss of generality, we assume that the domain of the i -th input variable, \mathcal{X}_i , is divided into K subintervals $\mathcal{X}_{i,j}$ ($j = 1, \dots, K$). Each $\mathcal{X}_{i,j}$ is referred to as a partition of the input domain and satisfies the following properties: (i) the partitions are mutually disjoint,

$$\mathcal{X}_{i,j} \cap \mathcal{X}_{i,l} = \emptyset, \quad \text{if } j \neq l, \quad (7)$$

and (ii) their union covers the entire input space,

$$\bigcup_{j=1}^K \mathcal{X}_{i,j} = \mathcal{X}_i. \quad (8)$$

Due to limited information, the exact probability measure \mathbb{P} of the inputs may be unknown. However, we assume that the statistical raw moments of the probability measure within each partition can be obtained. Without loss of generality, we further assume that all random inputs share the same number of available moments (denoted by r) in each subdomain. Accordingly, the information set \mathcal{A} can be expressed as

$$\mathcal{A} = \left\{ \mu \left| \mu = \bigotimes_{i=1}^m \mu_i, \int_{\mathcal{X}_{i,j}} x^{k-1} d\mu_i = M_{i,j,k-1}, i = 1, 2, \dots, m; j = 1, 2, \dots, K; k = 1, 2, \dots, r+1 \right. \right\}, \quad (9)$$

where μ_i denotes the probability measure of the i -th input and $M_{i,j,k-1}$ represents the $(k-1)$ -th raw truncated moment on the j -th subinterval of the i -th input. The zeroth raw moment corresponds to the probability mass, which is constrained by the normalization condition

$$\sum_{j=1}^K M_{i,j,0} = 1. \quad (10)$$

For notational simplicity, we assume in this work that all random inputs are partitioned into the same number of subdomains and that each subdomain is characterized by the same number of moment constraints. This assumption is made solely for clarity of presentation and does not restrict the generality of the proposed approach, which can be straightforwardly extended to cases where the number of subdomains or the number of prescribed moment constraints varies among input dimensions.

2.3. Reduction Theorem

All realizations in the information set \mathcal{A} defined in Eq. (9) are considered equally plausible representations of the underlying reality. Consequently, the most extreme scenarios within \mathcal{A} are of primary interest for UQ and certification. However, since the optimization problems in Eq. (6) are infinite-dimensional due to the uncountably many admissible probability measures μ , direct solutions are computationally intractable in practice.

To overcome this challenge, we employ the reduction theorem developed in Ref. [17], which builds upon Winkler's results on the extreme points of moment sets [18, 19]. Specifically, the reduction theorem reformulates the infinite-dimensional optimization problem into a finite-dimensional one expressed as a convex combination of Dirac measures. The partial information about uncertainties—namely, the raw moments defined over subdomains in Eq. (9)—is incorporated as constraints in the optimization problem. The theorem states that, for each random input, the number of Dirac supports and corresponding weights equals the number of equality constraints within each subdomain [17]. Consequently, the probability measure can be written as

$$\mu_i = \sum_{j=1}^K \sum_{k=1}^{r+1} t_{i,j,k} \delta_{x_{i,j,k}}, \quad i = 1, 2, \dots, m, \quad (11)$$

where $x_{i,j,k}$ and $t_{i,j,k}$ denote the k -th support and corresponding weight in the j -th subdomain of the i -th input, satisfying

$$\sum_{j=1}^K \sum_{k=1}^{r+1} t_{i,j,k} = 1, \quad \text{and} \quad x_{i,j,k} \in \mathcal{X}_{i,j}. \quad (12)$$

Since there are $r + 1$ moment constraints in each subdomain, the same number of supports and weights are required locally. The computation of the upper and lower bounds $U(\mathcal{A})$ and $L(\mathcal{A})$ is thus reduced to solving the finite-dimensional optimization problems

$$\begin{aligned} U(\mathcal{A})/L(\mathcal{A}) = \sup_{\{x\}, \{t\}} & \quad \sum_{\alpha_1=1}^{K(r+1)} \dots \sum_{\alpha_m=1}^{K(r+1)} \left(\prod_{i=1}^m t_{i,\alpha_i} \right) \mathbf{1}[G(x_{1,\alpha_1}, \dots, x_{m,\alpha_m}) \in \mathcal{Y}^c], \\ \text{subject to} & \quad x_{i,j,k} \in \mathcal{X}_{i,j}, \quad t_{i,j,k} \geq 0, \quad \sum_{l=1}^{r+1} t_{i,j,l} x_{i,j,l}^{k-1} = M_{i,j,k-1}, \\ & \quad i = 1, 2, \dots, m, \quad j = 1, 2, \dots, K, \quad k = 1, 2, \dots, r + 1, \end{aligned} \quad (13)$$

where $\{x\} \equiv \{x_{i,j,k} : i = 1, \dots, m; j = 1, \dots, K; k = 1, \dots, r + 1\} \in \mathbb{R}^{mk(r+1)}$ and $\{t\} \equiv \{t_{i,j,k} : i = 1, \dots, m; j = 1, \dots, K; k = 1, \dots, r + 1\} \in \mathbb{R}^{mk(r+1)}$. The variables x_{i,α_i} and t_{i,α_i} denote the flattened notations enumerating all Dirac supports and weights across subdomains, defined by

$$x_{i,\alpha_i} = x_{i,j,k}, \quad t_{i,\alpha_i} = t_{i,j,k}, \quad \text{where } \alpha_i = (r + 1)(j - 1) + k. \quad (14)$$

The flattened notation x_{i,α_i} and t_{i,α_i} is adopted in the objective function for conciseness, while the hierarchical form $x_{i,j,k}$ and $t_{i,j,k}$ is retained in the constraint expressions. The indicator function $\mathbf{1}[E]$ is defined as

$$\mathbf{1}[E] = \begin{cases} 1, & \text{if the statement } E \text{ is true,} \\ 0, & \text{otherwise.} \end{cases} \quad (15)$$

2.4. OUQ Solution

Two major challenges arise when solving the constrained optimization problem formulated in Eq. (13). The first challenge is the discrete nature of the objective function, i.e., the PoF, which is expressed as a sum of indicator functions that take binary values of either 0 or 1. This discreteness makes the direct application of gradient-based optimization methods infeasible. The second challenge lies in the enforcement of moment constraints representing partial information about the input variables. This becomes particularly difficult when a large number of equality constraints are imposed, as derivative-free algorithms often struggle to efficiently satisfy them.

To address these challenges, several numerical strategies have been developed. The first is the Mystic framework [35], which employs a nested (two-level) optimization scheme — an outer loop that minimizes or maximizes the PoF and an inner loop that identifies feasible candidates that satisfy the imposed constraints. Both loops rely on derivative-free optimizers such as Differential Evolution (DE) [36]. The second approach introduces a neural-network-based approximation of the indicator functions [37], leveraging their similarity to classification problems in machine learning. This learning-based OUQ formulation enables the use of efficient gradient-based algorithms to solve the resulting optimization problem, wherein the constrained formulation is transformed into an unconstrained one through penalty methods. The third strategy utilizes canonical moments to reformulate the OUQ problem [34]. In this work, since a large number of moment constraints are imposed, both the Mystic framework and penalty-based methods become inefficient. The Mystic framework struggles to sufficiently explore the feasible constrained space within the inner loop, while the penalty-based methods introduce significant numerical errors due to the large penalty terms dominating the objective function. Consequently, we employ the canonical-moment-based approach to efficiently and accurately solve Eq. (13), which has demonstrated superior performance in handling moment-constraint optimization problems in OUQ [34].

Canonical moments can be interpreted as the relative positions of classical moments within their admissible moment spaces [38]. They are defined on the interval $[0, 1]$, and any finite sequence of classical moments can be transformed into an equivalent sequence of canonical moments of the same order. The key idea of the canonical-moment-based approach is to convert the constrained optimization problem, originally formulated in terms of the Dirac supports $\{x\}$ and weights $\{t\}$, into an unconstrained optimization problem parameterized by a set of canonical moments of higher order than those appearing in the constraints. These canonical moments, treated as optimization variables, are referred to as *free canonical moments*. The moment constraints are enforced by constructing a polynomial function using *fixed canonical moments*, which are derived from the given moment constraints. The roots of this polynomial correspond to the Dirac supports $\{x\}$, and the associated weights $\{t\}$ are subsequently determined by solving the linear system defined by the moment constraint equations. This canonical-moment-based formulation preserves the feasibility of the constraint space, ensuring nonnegativity of the Dirac weights, containment of supports within the prescribed subdomains, and exact satisfaction of the moment-matching conditions.

For each subdomain $\mathcal{X}_{i,j}$ and its corresponding truncated moments $M_{i,j,k-1}$, the optimization problem is reformulated using canonical moments through the following steps: (1) transform the raw moments from the original subdomain $\mathcal{X}_{i,j}$ to the unit interval $[0, 1]$; (2) compute the first r fixed canonical moments from the given moment constraints and augment them with $r+1$ free canonical moments that serve as optimization variables; (3) construct a tridiagonal Jacobi matrix whose eigenvalues correspond to the Dirac supports and whose eigenvectors determine the Dirac weights; (4) map the resulting discrete measure back to the original subdomain $\mathcal{X}_{i,j}$; (5) formulate a constraint-free optimization problem in terms of these free canonical moments; and (6) reduce the number of indicator-function evaluations in the PoF calculation by ITS.

2.4.1. Affine Transformation to the Unit Interval

We first transform random inputs and the corresponding truncated raw moments from the original subdomain $\mathcal{X}_{i,j}$ to the unit interval $[0, 1]$. Specifically, each random input is affinely scaled using the min-max normalization

$$\xi_i = \frac{x_i - a_{i,j}}{b_{i,j} - a_{i,j}}, \quad x_i \in \mathcal{X}_{i,j}, \quad (16)$$

where $a_{i,j}$ and $b_{i,j}$ denote the lower and upper bounds of $\mathcal{X}_{i,j}$, respectively, and $\xi_i \in [0, 1]$ represents the normalized variable corresponding to the random input x_i . The truncated raw moments are then transformed using a binomial

expansion

$$\tilde{M}_{i,j,k-1} = \frac{1}{(b_{i,j} - a_{i,j})^{k-1}} \sum_{l=0}^{k-1} \binom{k-1}{l} (-a_{i,j})^{k-l-1} M_{i,j,l}, \quad k = 1, \dots, r+1. \quad (17)$$

This affine transformation serves two primary purposes. First, it normalizes the total probability mass over the subdomain $\mathcal{X}_{i,j}$, ensuring that $\tilde{M}_{i,j,0} = 1$. Second, it standardizes the supports to the unit interval $[0, 1]$, on which the theory of canonical moments is defined. By construction, each $\tilde{M}_{i,j,k-1}$ represents the $(k-1)$ -th raw moment of a probability measure on $[0, 1]$ corresponding to the original truncated measure on $\mathcal{X}_{i,j}$.

2.4.2. Computation of Canonical Moments

Given a sequence of $r+1$ raw moment constraints $\tilde{M}_{i,j,k-1}$ ($k = 1, \dots, r+1$) defined over the subdomain $\mathcal{X}_{i,j}$, the corresponding fixed canonical moments $p_{i,j,k-1}$ ($k = 1, \dots, r+1$) can be computed. The analytical expressions for the first three moments ($k = 1, 2, 3$) are available

$$p_{i,j,0} = 0, \quad p_{i,j,1} = \tilde{M}_{i,j,1}, \quad p_{i,j,2} = \frac{\tilde{M}_{i,j,2} - (\tilde{M}_{i,j,1})^2}{\tilde{M}_{i,j,1}(1 - \tilde{M}_{i,j,1})}. \quad (18)$$

For higher-order moments, the corresponding canonical moments can be computed using two classical algorithms. The first is based on Hankel determinants, in which a sequence of square Hankel matrices is constructed from the raw moments, and the canonical moments are derived from the determinants of these matrices [38]. However, this approach requires evaluating many Hankel determinants and is therefore computationally expensive and potentially numerically unstable. To overcome this issue, a more efficient alternative is the Quotient-Difference (Q-D) algorithm [39, 40], which recursively generates a triangular array—known as the Q-D table [38]—and yields the canonical moments with significantly improved numerical efficiency. It is important to note that enforcing the original moment constraints $M_{i,j,k-1}$ ($k = 1, \dots, r+1$) or their canonical counterparts $p_{i,j,k-1}$ ($k = 1, \dots, r+1$) is mathematically equivalent in terms of moment matching.

Once the first $r+1$ fixed canonical moments $p_{i,j,k-1}$ have been determined, they are augmented by an additional set of $r+1$ higher-order canonical moments, $p_{i,j,k-1}$ ($k = r+2, \dots, 2r+2$), which serve as optimization variables in the OUQ problem. These free canonical moments take values in the interval $(0, 1)$, which ensures that the resulting measure remains admissible within the moment space.

2.4.3. Solution of Supports and Weights via Eigendecomposition

Given the canonical moment sequence $p_{i,j,k-1}$ ($k = 1, \dots, 2r+2$) associated with the subdomain $\mathcal{X}_{i,j}$, we seek to construct an $(r+1)$ -point Dirac measure $\tilde{\mu}_{i,j} = \sum_{k=1}^{r+1} \omega_{i,j,k} \delta_{\xi_{i,j,k}}$ supported on $[0, 1]$, whose first $r+1$ moments match the transformed moment constraints $\tilde{M}_{i,j,k-1}$ ($k = 1, \dots, r+1$). Here, $\xi_{i,j,k}$ and $\omega_{i,j,k}$ denote the Dirac supports and weights, respectively. Following [20], the supports $\xi_{i,j,k}$ ($k = 1, \dots, r+1$) coincide with the roots of a polynomial $P_{(r+1)}$ of degree $r+1$, which is generated through the three-term recurrence relation

$$P_{(k+1)}(\xi) = (\xi - (\zeta_{2k+1} + \zeta_{2k+2})) P_{(k)}(\xi) - \zeta_{2k} \zeta_{2k+1} P_{(k-1)}(\xi), \quad k = 0, 1, \dots, r, \quad (19)$$

with the initial polynomials $P_{(-1)} := 0$ and $P_{(0)} := 1$. The recurrence coefficients ζ_k over $\mathcal{X}_{i,j}$ are defined as

$$\zeta_k := p_{i,j,k-1} (1 - p_{i,j,k}), \quad \zeta_0 := 0, \quad \zeta_{2r+2} := 0. \quad (20)$$

Once the supports $\xi_{i,j,k}$ are computed as the roots of $P_{(r+1)}$, the weights $\omega_{i,j,k}$ are obtained by enforcing the moment-matching conditions

$$\sum_{k=1}^{r+1} \omega_{i,j,k} \xi_{i,j,k}^{l-1} = \tilde{M}_{i,j,l-1}, \quad l = 1, 2, \dots, r+1. \quad (21)$$

Eq. (21) forms a linear system in unknown weights $\omega_{i,j,k}$, whose coefficient matrix is a Vandermonde matrix constructed from the supports $\xi_{i,j,k}$. This system is invertible as long as all supports $\xi_{i,j,k}$ are distinct. However, the

polynomial-based computation of the supports can become unstable when two or more roots are very close together or coincide. In such cases, the Vandermonde matrix becomes ill-conditioned, leading to substantial numerical errors in the recovered weights.

Alternatively, in this work we employ an eigendecomposition-based procedure known as the Golub-Welsch algorithm [41]. A symmetric tridiagonal Jacobi matrix $J_{i,j}$ over $\mathcal{X}_{i,j}$ is constructed from the recurrence coefficients

$$J_{i,j} = \begin{bmatrix} \zeta_1 + \zeta_2 & \sqrt{\zeta_2 \zeta_3} & & & \\ \sqrt{\zeta_2 \zeta_3} & \zeta_3 + \zeta_4 & \ddots & & \\ & \ddots & \ddots & & \\ & & \sqrt{\zeta_{2r} \zeta_{2r+1}} & \sqrt{\zeta_{2r} \zeta_{2r+1}} & \\ & & & \zeta_{2r+1} + \zeta_{2r+2} & \end{bmatrix} \in \mathbb{R}^{(r+1) \times (r+1)}. \quad (22)$$

The eigenvalues of the Jacobi matrix $J_{i,j}$ equal to the Dirac supports $\xi_{i,j,k}$, while the corresponding weights are obtained from the normalized eigenvectors

$$\omega_{i,j,k} = v_{k,1}^2, \quad (23)$$

where $v_{k,1}$ is the first component of the k -th eigenvector.

Constructing the Jacobi matrix requires canonical moments up to order $2r + 2$: the first $r + 1$ fixed canonical moments, derived from the truncated moment constraints, and additional $r + 1$ free canonical moments of higher order. Any admissible choice of these free moments $p_{i,j,k-1}$ ($k = r + 2, \dots, 2r + 2$), together with the fixed moments $p_{i,j,k-1}$ ($k = 1, \dots, r + 1$), uniquely determines a probability measure satisfying the moment-matching conditions in Eq. (21). Thus, these higher-order canonical moments serve as the optimization variables in the resulting constraint-free OUQ formulation. Because canonical moments are naturally bounded within $[0, 1]$, admissible candidate solutions are straightforward to generate, in contrast to the classical-moment representation.

From a numerical standpoint, the eigendecomposition-based procedure replaces the polynomial root-finding step with the eigendecomposition of a real, symmetric, tridiagonal matrix—a well-conditioned problem for which fast and stable algorithms are readily available. In addition, the corresponding eigenvectors directly provide the Dirac weights, thereby eliminating the need to solve a potentially ill-conditioned Vandermonde system.

2.4.4. Recovery of Supports and Weights

Once the Dirac supports $\xi_{i,j,k}$ and weights $\omega_{i,j,k}$ on the unit interval $[0, 1]$ are obtained via the eigendecomposition of the Jacobi matrix, they are mapped back to the original subdomain $\mathcal{X}_{i,j}$ using

$$x_{i,j,k} = a_{i,j} + (b_{i,j} - a_{i,j}) \xi_{i,j,k}, \quad t_{i,j,k} = M_{i,j,0} \omega_{i,j,k}, \quad i = 1, \dots, m, \quad j = 1, \dots, K, \quad k = 1, \dots, r + 1. \quad (24)$$

The recovered supports $x_{i,j,k}$ and weights $t_{i,j,k}$ on the original subdomain are then supplied to the forward model F for the evaluation of the PoF.

2.4.5. Constraint-Free Optimization over Canonical Moments

After transforming the classical moments into canonical moments and introducing additional higher-order canonical moments, the constrained OUQ problem in Eq. (13) can be reformulated as an unconstrained optimization problem over a hypercube with the following objective function

$$\text{PoF}(\{p\}^{\text{free}}) = \sum_{\alpha_1=1}^{K(r+1)} \cdots \sum_{\alpha_m=1}^{K(r+1)} \left(\prod_{i=1}^m t_{i,\alpha_i}(\{p\}) \right) \mathbf{1} \left[G(x_{1,\alpha_1}(\{p\}), \dots, x_{m,\alpha_m}(\{p\})) \in \mathcal{Y}^c \right], \quad (25)$$

where

$$\{p\}^{\text{free}} \equiv \{p_{i,j,k-1} : i = 1, \dots, m; j = 1, \dots, K; k = r + 2, \dots, 2r + 2\} \in (0, 1)^{mk(r+1)}$$

denotes the free higher-order canonical moments, and

$$\{p\} \equiv \{p_{i,j,k-1} : i = 1, \dots, m; j = 1, \dots, K; k = 1, \dots, 2r + 2\}$$

contains both fixed and free canonical moments. The mappings from canonical moments to Dirac supports $x_{i,\alpha_i}(\{p\})$ and weights $t_{i,\alpha_i}(\{p\})$ are performed following the procedures in Sections 2.4.1-2.4.4.

It is important to note that this canonical-moment reformulation does not alter the discrete nature of the objective function, which still involves indicator functions. However, it dramatically reduces the number of optimization variables. Only $mK(r+1)$ free canonical moments are optimized, compared with the original formulation requiring $mK(r+1)$ Dirac supports and $mK(r+1)$ associated weights—a total of $2mK(r+1)$ variables. As a result, this approach not only converts the problem into a fully constraint-free optimization but also substantially decreases the dimensionality of the search space, leading to a more efficient and numerically stable optimization procedure.

2.4.6. Model Reduction via Inverse Transform Sampling

The objective function in the constraint-free OUQ formulation given in Eq. (25) requires $(K(r+1))^m$ evaluations of the forward map and its associated indicator function to compute a single PoF value. Consequently, the computational cost can become prohibitive, especially for high-dimensional problems. For example, in our numerical study with $K = 8$, $r = 2$, and $m = 5$, computing a single PoF evaluation would require nearly eight million forward-map and indicator-function evaluations.

To mitigate this cost, we approximate the PoF through ITS [42, 43], a classical method for generating random samples from an arbitrary probability distribution using its cumulative distribution function (CDF). For the discrete Dirac measure in Eq. (11), the CDF of the i -th random input is

$$F_i(x) = \sum_{j=1}^{K-1} \sum_{k=1}^{r+1} t_{i,j,k} \mathbf{1}[x_{i,j,k} \leq x]. \quad (26)$$

We draw samples via the ITS method by generating i.i.d. random numbers from a uniform distribution on $[0, 1]$, i.e., $c_l \sim \text{Unif}[0, 1]$ for $l = 1, 2, \dots, N_{\text{ITS}}$, where N_{ITS} denotes the number of inverse-transform samples. The l -th sample of the i -th input is then obtained by

$$X_i^{(l)} = \inf \{x : F_i(x) \geq c_l\}, \quad i = 1, 2, \dots, m, \quad (27)$$

which corresponds to selecting the smallest Dirac support whose cumulative weight exceeds the uniform draw. Fig. 2 schematically illustrates the ITS procedure using a three-point Dirac measure as an example. With these sampled inputs, the PoF is approximated through Monte Carlo estimation

$$\text{PoF}(\{p\}^{\text{free}}) \approx \frac{1}{N_{\text{ITS}}} \sum_{l=1}^{N_{\text{ITS}}} \mathbf{1}[G(X_1^{(l)}, \dots, X_m^{(l)}) \in \mathcal{Y}^c]. \quad (28)$$

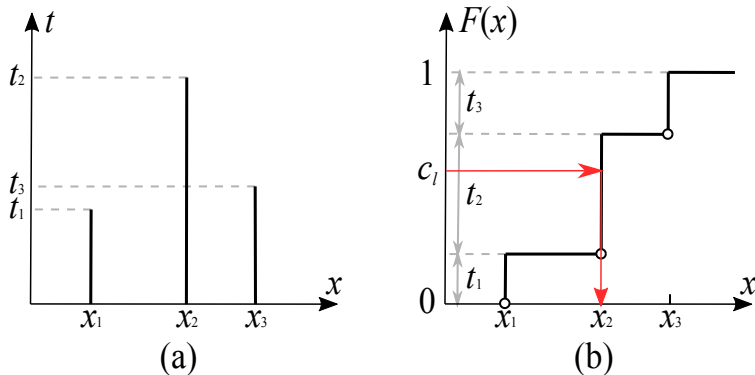


Figure 2: Illustration of ITS in OUQ: (a) PDF of a three-point Dirac measure, and (b) Corresponding CDF and ITS.

An additional motivation for using ITS arises from examining how each term of the joint Dirac measure contributes to the PoF. As shown in Eq. (25), the Dirac supports determine whether a term contributes, while the Dirac weights determine the magnitude of that contribution. The contribution of a joint term is on the order of $O(t^m)$, where t denotes

a representative weight. Thus, for large m , contributions from terms with small weights become negligible. In other words, computational effort should focus on combinations with relatively large weights. As illustrated in Fig. 2(b), ITS automatically emphasizes these dominant terms (e.g., t_1 compared with t_2 in Fig. 2(b)). Dirac supports with larger weights are selected more frequently, while those with very small weights are rarely sampled.

To compute a single PoF value, the ITS approach requires N_{ITS} evaluations of the forward map and its associated indicator function. The accuracy of ITS also depends on the number of samples: larger sample sizes generally yield more accurate approximations. However, for low-dimensional problems, the cost of ITS may exceed that of directly evaluating the PoF using all Dirac combinations, since $(K(r+1))^m$ may be smaller than N_{ITS} . Therefore, we introduce a threshold to decide whether ITS should be used. Specifically, if $(K(r+1))^m < N_{\text{ITS}}$, we compute the PoF exactly using the original Dirac measure. Otherwise, when $(K(r+1))^m \geq N_{\text{ITS}}$, we employ ITS with N_{ITS} samples to approximate the PoF.

Moreover, to stabilize the search for extremal PoF values, we employ the Common Random Numbers (CRN) variance reduction technique [44, 45]. A single large vector of uniform random numbers is generated once and reused for the sampling step of every candidate measure evaluated. This induces positive correlation between the PoF estimates of similar candidates, reducing the variance of their differences and enabling a more reliable and efficient optimization process.

2.5. Implementation Details

The OUQ methodology computes the extremal PoF values by optimizing over combinations of Dirac measures subject to truncated moment constraints. Algorithm 1 outlines the procedure for evaluating the objective function, namely, the PoF, in the resulting unconstrained canonical-moment formulation. It is important to emphasize that the inputs to the optimization algorithm are the $mK(r+1)$ free canonical moments associated with all input variables, each taking values in the interval $(0, 1)$.

In this work, we employ DE [36] to search over the space of free canonical moments. DE is a population-based, derivative-free, stochastic optimization algorithm that is particularly well suited for OUQ. It handles the non-smooth, discontinuous nature of the indicator function in the PoF computation, naturally enforces simple box constraints, and performs reliably on global optimization problems with multiple local optima [46]. At each iteration, DE mutates and recombines a population of candidate solutions, decodes each candidate into Dirac supports and weights via Algorithm 1, evaluates the corresponding PoF, and selects the best-performing candidates for the next generation. The procedure is repeated until convergence or until a prescribed maximum number of iterations is reached. In our implementation, the population size is chosen to be between 20 and 50 times the number of optimization variables, and the maximum number of iterations is set between 100 and 200, which was found to provide a good balance between convergence robustness and computational efficiency.

3. A Special Case: OUQ under Zeroth-Order Moment Constraints

The OUQ framework under general moment constraints offers a powerful and flexible approach for modeling uncertainty and quantifying its impact on system outputs. It is natural to compare this framework with other established uncertainty models. To this end, in this section we examine a special case in which the uncertain inputs are constrained only by zeroth-order moments. We show that, under this setting, the resulting OUQ formulation becomes equivalent to the evidence theory [10, 11].

We assume that the zeroth moments, i.e., the probabilities of the input lying in each subdomain, are known. As a result, the information set \mathcal{A} can be written as

$$\mathcal{A} = \left\{ \mu \left| \mu = \bigotimes_{i=1}^m \mu_i, \mu_i[X_i \in \mathcal{X}_{i,j}] = M_{i,j,0}, i = 1, \dots, m; j = 1, \dots, K \right. \right\}. \quad (29)$$

A schematic illustration of partitioning the domain of a one-dimensional random input is shown in Fig. 3. Our goal is to compute upper and lower bounds on $\mathbb{P}[Y \in \mathcal{Y}^c]$ based on the available information in Eq. (29). For any probability measure μ , the PoF can be expressed as

$$\mu[Y \in \mathcal{Y}^c] = \mu[X \in \mathcal{X}^c], \quad (30)$$

where \mathcal{X}^c is the failure domain in the input space

$$\mathcal{X}^c \equiv \{X \mid G(X) \in \mathcal{Y}^c\} \subseteq \mathcal{X}. \quad (31)$$

Algorithm 1 Calculation of PoF as a function of free canonical moments

- 1: **Input:** Free canonical moments $p_{i,j,k+r+1}$; subdomains $\mathcal{X}_{i,j}$; truncated moments $M_{i,j,k-1}$ ($i = 1, \dots, m$, $j = 1, \dots, K$, $k = 1, \dots, r+1$); forward mapping G ; inadmissible set \mathcal{Y}^c ; number of inverse-transform samples N_{ITS}
- 2: **Begin**
- 3: **for** $i = 1, \dots, m$ **do**
- 4: **for** $j = 1, \dots, K$ **do**
- 5: (a) Map the subdomain $\mathcal{X}_{i,j}$ to $[0, 1]$ and compute the transformed moments $\tilde{M}_{i,j,k-1}$ using Eq. (17)
- 6: (b) Compute fixed canonical moments $p_{i,j,k}$ ($k = 1, \dots, r+1$) using Eq. (18) or the Q-D algorithm
- 7: (c) Augment the fixed canonical moments with free canonical moments $p_{i,j,k}$ ($k = r+2, \dots, 2r+2$) to obtain the full sequence $p_{i,j,k}$ ($k = 1, \dots, 2r+2$)
- 8: (d) Compute recurrence coefficients via Eq. (20) and construct the Jacobi matrix $J_{i,j}$ using Eq. (22)
- 9: (e) Eigendecompose $J_{i,j}$ to obtain Dirac supports $\xi_{i,j,k}$ and weights $\omega_{i,j,k}$ using Eq. (23)
- 10: (f) Recover original supports $x_{i,j,k}$ and weights $t_{i,j,k}$ using Eq. (24)
- 11: **if** $(K(r+1))^m < N_{\text{ITS}}$ **then**
- 12: Compute PoF exactly using Eq. (25)
- 13: **else**
- 14: **for** $i = 1, \dots, m$ **do**
- 15: Generate N_{ITS} uniform random samples on $[0, 1]$
- 16: Generate N_{ITS} samples of the i -th input using Eq. (27)
- 17: Estimate PoF using Eq. (28)
- 18: **End**
- 19: **Output:** PoF($\{p\}^{\text{free}}$)

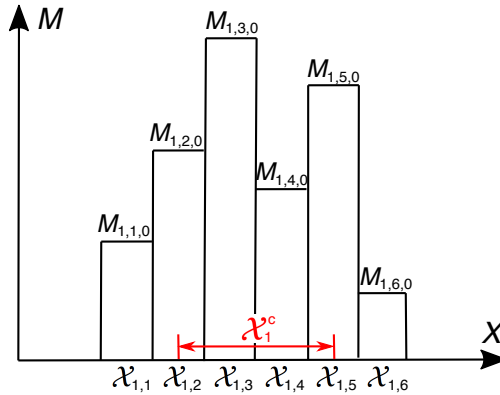


Figure 3: Schematic illustration of the probability constraints for a one-dimensional random variable. The input domain is partitioned into subintervals $\mathcal{X}_{i,j}$, and the failure region \mathcal{X}_i^c is highlighted for comparison. In this example, the upper and lower bounds on the PoF are $U = M_{1,2,0} + M_{1,3,0} + M_{1,4,0} + M_{1,5,0}$ and $L = M_{1,3,0} + M_{1,4,0}$, respectively.

Since the random inputs are independent, the failure domain can be decomposed as

$$\mathcal{X}^c = \prod_{i=1}^m \mathcal{X}_i^c, \quad (32)$$

where \mathcal{X}_i^c denotes the failure set corresponding to the i -th input variable. The upper and lower bounds on the PoF over the information set \mathcal{A} follow as

$$U(\mathcal{A}) = \prod_{i=1}^m \sum_{j=1}^K M_{i,j,0} \mathbf{1}[\mathcal{X}_i^c \cap \mathcal{X}_{i,j} \neq \emptyset], \quad (33a)$$

$$L(\mathcal{A}) = \prod_{i=1}^m \sum_{j=1}^K M_{i,j,0} \mathbf{1}[\mathcal{X}_i^c \cap \mathcal{X}_{i,j} = \mathcal{X}_{i,j}]. \quad (33b)$$

A detailed derivation of Eq. (33) is provided in Appendix A. In words, the upper bound sums the probabilities of all subdomains $\mathcal{X}_{i,j}$ that intersect the failure region \mathcal{X}_i^c , whereas the lower bound sums the probabilities of those subdomains entirely contained in the failure region. These quantities correspond to the *plausibility* and *belief* functions in the evidence theory [10, 11]. An example of these bounds is illustrated in Fig. 3.

4. Numerical Examples

In this section, we present three numerical examples to evaluate the effectiveness of the proposed subdomain-based OUQ methodology and computational framework. The first example considers identity functions of four basic distributions to illustrate the resulting PoF bounds. The second example examines a five-dimensional nonlinear problem to assess the numerical techniques incorporated in the OUQ framework. Finally, the third example applies the framework to an engineering-related ballistic impact problem, investigating how varying levels of uncertainty in material properties influence the UQ of the ballistic performance of a magnesium alloy plate.

In all examples, the forward mapping G produces a single output with a maximum allowable threshold Y^c , and the inadmissible set is therefore $\mathcal{Y}^c = [Y^c, +\infty)$. Although the true distributions of inputs and their corresponding PDFs are specified for each example, in the OUQ setting we assume that these PDFs are unknown. The truncated moments required by OUQ are computed using the true PDFs solely for the purpose of benchmarking. Moreover, we consider only equally partitioned input domains, though the methodology can be straightforwardly extended to accommodate non-equally partitioned domains.

4.1. Case 1: Identity Functions of One-Dimensional Problems

We consider the case in which the mapping G is an identity function defined over a bounded one-dimensional domain, i.e., $G(X) = X$ for $X \in [a, b]$. Four basic probability distributions are examined: the normal, uniform, Weibull, and bimodal normal-mixture distributions. Each distribution is further truncated to the input domain $[a, b]$ according to

$$f^*(x) = \frac{f(x)}{F(b) - F(a)} \mathbf{1}[x \in [a, b]], \quad (34)$$

where $f(x)$ and $F(x)$ denote the PDF and CDF of the original untruncated distribution. Table 1 summarizes the original PDF $f(x)$, the input domain $[a, b]$, the output threshold Y^c , and the true PoF. Fig. 4 illustrates the truncated PDFs and the corresponding failure domains for the four distributions. In this one-dimensional example, ITS is not employed. Instead, the PoF in OUQ is computed exactly using Eq. (25).

Table 1
Summary of the four one-dimensional problems.

Distribution	$f(x)$	$[a, b]$	Y^c	True PoF
Normal	$\phi(x; 0, 1)$	$[-5, 5]$	0.7	0.2420
Uniform	0.1	$[-5, 5]$	1.7	0.3300
Weibull	$\frac{k}{\lambda} \left(\frac{x}{\lambda}\right)^{k-1} e^{-(x/\lambda)^k}$ with $k=1.5$ and $\lambda=2$	$[0, 10]$	3.0	0.1593
Bimodal normal-mixture	$0.35 \phi(x; -2, 1) + 0.65 \phi(x; 2, 1)$	$[-5, 5]$	1.3	0.4927

Notes: (i) $\phi(x; m, s) = \frac{1}{\sqrt{2\pi}s} \exp\left(-\frac{(x-m)^2}{2s^2}\right)$. (ii) The true PoF is calculated by quadrature.

The input domains of the four test cases are partitioned into $K = 1, 2, 4$, and 8 subdomains. We consider moment constraints up to the third order, i.e., $r = 0, 1, 2$, and 3. Recall that the case $r = 0$ corresponds to the setting of the evidence theory. Fig. 5 presents the true PoF, along with its optimal upper and lower bounds obtained from the proposed OUQ framework. The numerical values of these optimal bounds are summarized in Tables 6-9 in Appendix C.

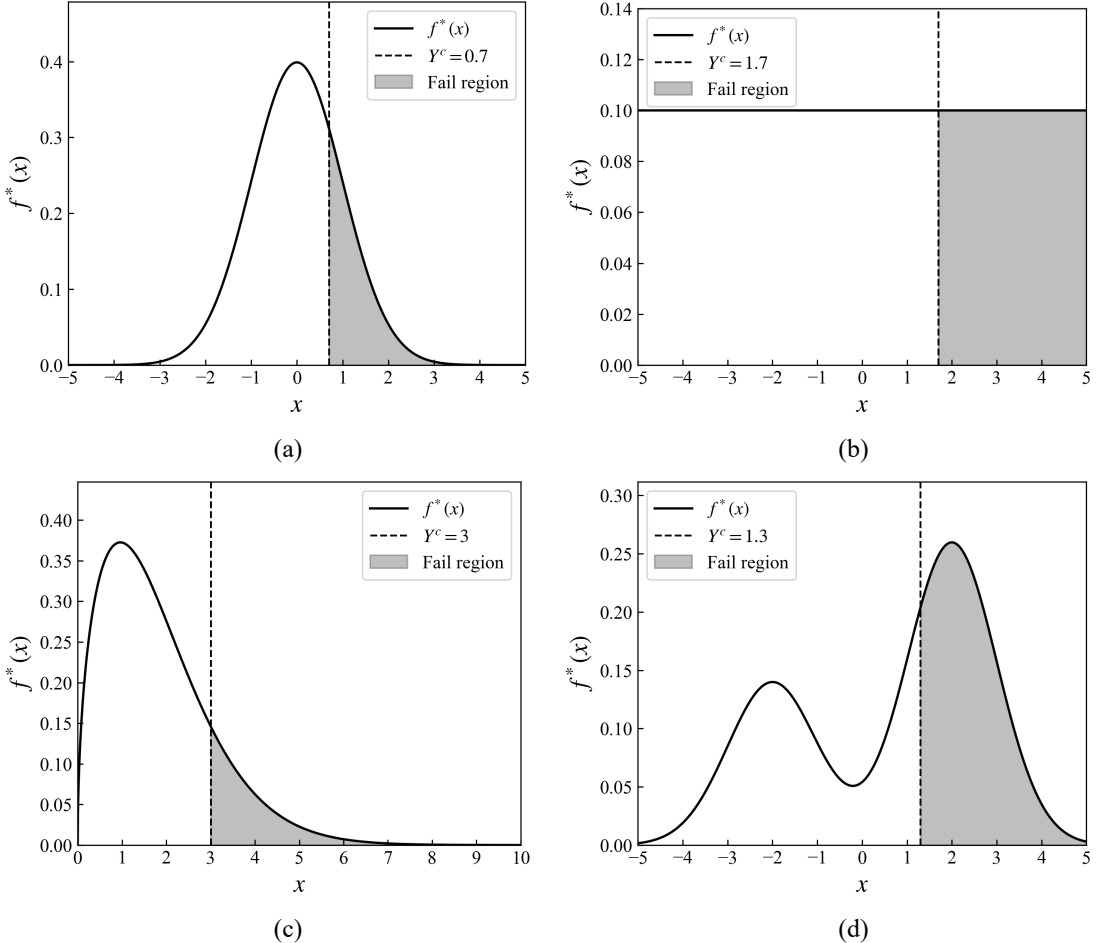


Figure 4: Truncated PDFs and corresponding failure regions for the four considered distributions: (a) truncated normal, (b) uniform, (c) truncated Weibull, and (d) truncated bimodal normal-mixture.

A clear trend observed in Fig. 5 is that the upper bound U decreases and the lower bound L increases as either the number of subdomains or the number of moment constraints increases. Consequently, the gap between U and L shrinks as additional uncertainty information is incorporated. Importantly, for all test cases, the true PoF is consistently bracketed by the two optimal bounds. Since these bounds are optimal given the available information, further tightening requires incorporating additional knowledge about the uncertainties. As expected, in the limit of sufficiently many subdomains or higher-order moment constraints, both U and L should converge closely to the true PoF. Thus, enriching the available uncertainty information enhances the tightness of the PoF bounds.

More specifically, the four distributions yield different optimal bounds for the same values of K and r , except in certain extreme cases where $U = 1$ or $L = 0$, which correspond to scenarios with minimal uncertainty information and therefore uninformative bounds. The tightest bounds are obtained when the uncertainty information is richest, i.e., at $K = 8$ and $r = 3$. The resulting optimal bounds are $[L, U] = [0.1436, 0.3556]$ for the normal distribution, $[0.2963, 0.3608]$ for the uniform distribution, $[0.1098, 0.2148]$ for the Weibull distribution, and $[0.4467, 0.5027]$ for the bimodal normal-mixture distribution. These intervals deviate from their respective true PoFs by $[-40.66\%, +46.94\%]$, $[-10.21\%, +9.33\%]$, $[-31.05\%, +34.87\%]$, and $[-9.34\%, +2.03\%]$. Therefore, among the four cases, the uniform and bimodal normal-mixture distributions show the greatest sensitivity to additional uncertainty information, the normal distribution shows the least sensitivity, and the Weibull distribution exhibits intermediate behavior.

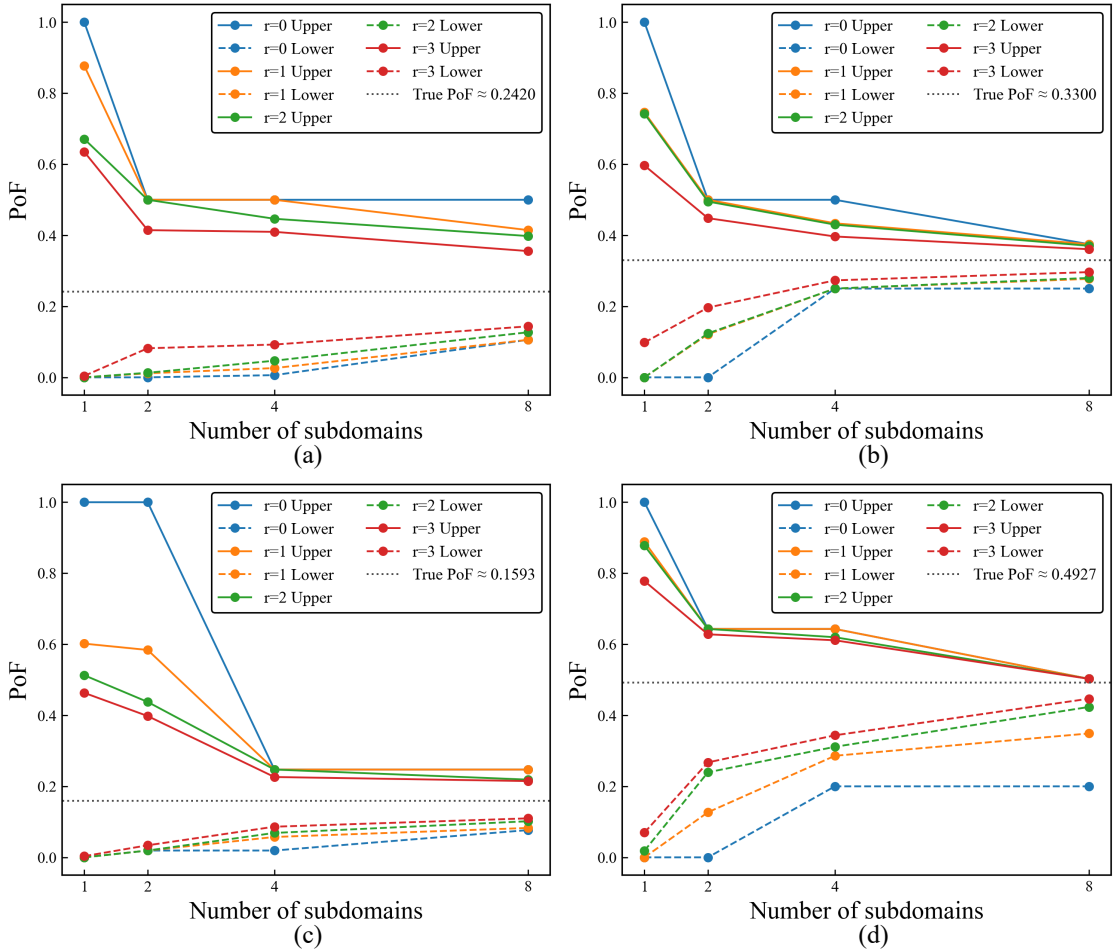


Figure 5: Optimal PoF bounds as functions of the number of subdomains and moment constraints: (a) truncated normal, (b) uniform, (c) truncated Wei-bull, and (d) truncated bimodal normal-mixture.

An additional observation in Fig. 5 is that increasing the number of subdomains or moment constraints does not always strictly decrease the upper bound or increase the lower bound. This behavior arises from the simplicity of the identity mapping considered in this example. When the additional uncertainty information pertains to regions of the input space that lie entirely within either the safe domain or the failure domain, it does not affect the PoF bounds, which are primarily governed by the probability mass near the boundary between the safe and failure domains, as illustrated in Fig. 4.

To illustrate how uncertainty information influences the extremal measures, Fig. 6 compares the Dirac CDFs obtained at the optimal bounds for the cases $K = 1$ and $K = 8$ (both with $r = 2$) against the corresponding true probability CDFs. In these CDF plots, the supports of the Dirac measures appear as the locations of the step changes, while the height of each step represents the associated Dirac weight. As expected, as more information about the true measure is incorporated, the optimal-bound CDFs increasingly resemble the true CDF in all four cases. More uncertainty information leads to Dirac CDFs with more steps, yielding extremal measures that more closely approximate the true probability measures. It is also important to note, as shown in Fig. 6, that the obtained Dirac measures are extremal only with respect to the targeted PoF. They do *not* provide optimal bounds on the CDF over its entire domain, in contrast to the behavior typically observed in p-box formulations [12].

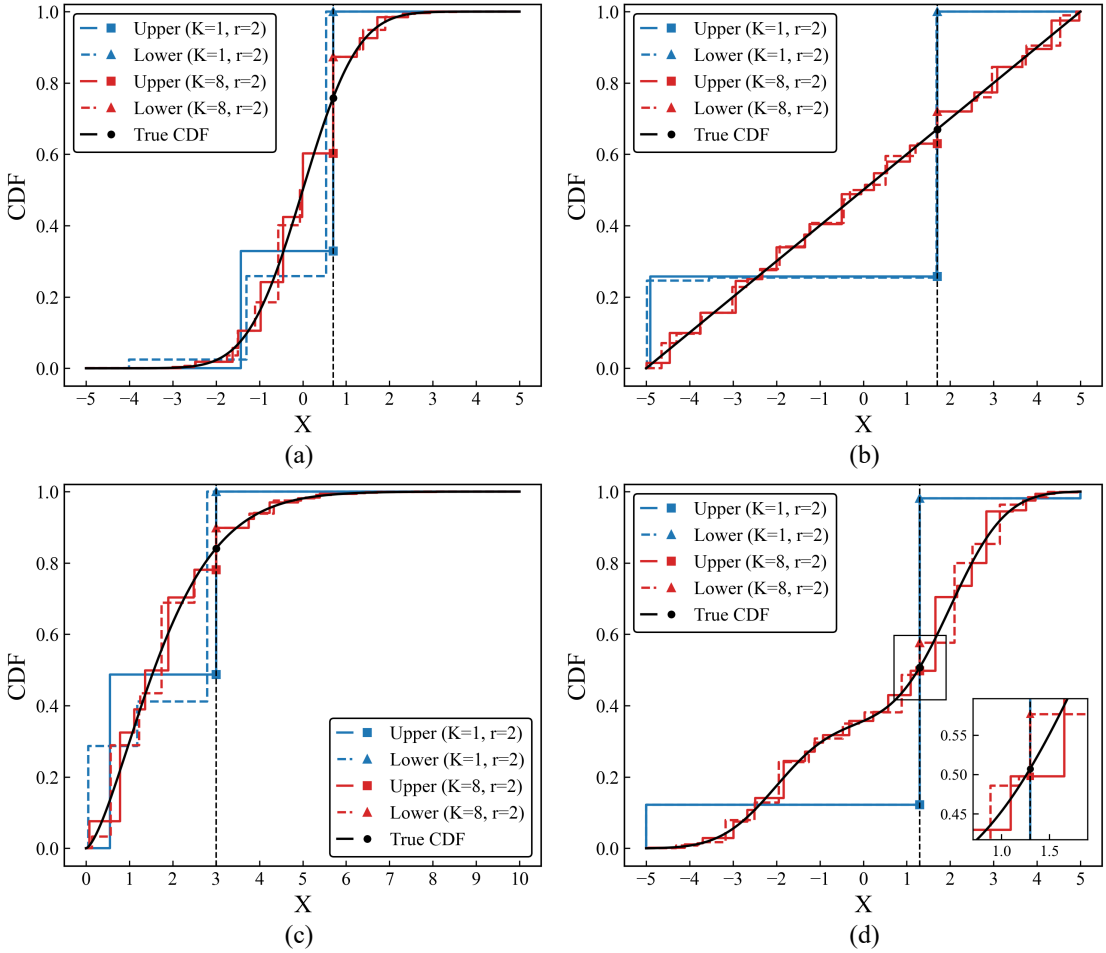


Figure 6: Comparison between the Dirac CDFs at the optimal bounds and the corresponding true CDFs: (a) truncated normal, (b) uniform, (c) truncated Wei-bull, and (d) truncated bimodal normal mixture.

4.2. Case 2: A Five-Dimensional Nonlinear Problem

We next consider a more complex five-dimensional nonlinear problem. The forward mapping G is defined as

$$G(X) = 0.7X_1 + 0.35X_2^2 - 0.25X_3X_4 + \frac{0.2X_3^2}{1 + X_3^2} + \sin(X_5), \quad (35)$$

where $X \equiv (X_1, \dots, X_5)$. The failure threshold for the output is $Y^c = 0.8$. Each random input X_i ($i = 1, \dots, 5$) is assumed to follow a truncated normal distribution computed using Eq. (34). The input domains and the corresponding untruncated PDFs are summarized in Table 2.

The input domains of the five variables are partitioned into $K = 1, 2, 4$, and 8 subdomains simultaneously. We consider moment constraints up to the second order, i.e., $r = 0, 1$, and 2 . Recall that a single exact evaluation of the PoF requires $(K(r+1))^m$ evaluations of the forward mapping. In this example, $m = 5$, so the exact computation becomes extremely expensive and even infeasible for large values of K and r . Consequently, in these computationally prohibitive cases we employ the ITS method described in Section 2.4.6 to estimate the PoF within the OUQ framework. To determine an appropriate number of inverse-transform samples, we first examine how the PoF varies with the number of samples N_{ITS} for two representative cases: $K = 4$ and $K = 8$ both with $r = 2$. For this comparison, we fix the free canonical moments $\{p\}^{\text{free}}$ and hence the corresponding Dirac measures, and compute the resulting PoF.

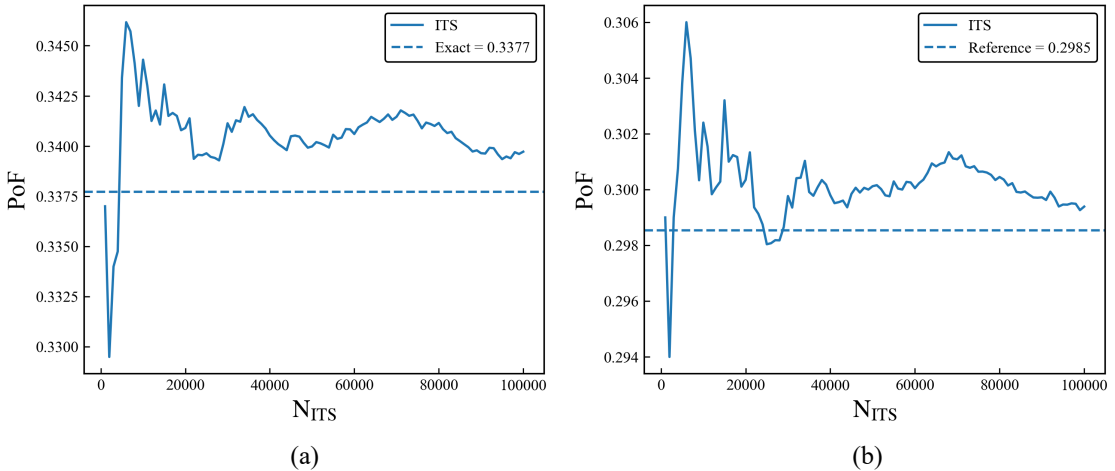
Fig. 7 shows the PoF as a function of N_{ITS} for these two cases. For the first case, Fig. 7(a), we also compute the exact PoF using Eq. (25), which requires 248,832 evaluations of the forward mapping. As expected, the estimate obtained

Table 2

Summary of the inputs for the five-dimensional nonlinear problem.

Input	$f(x)$	$[a, b]$
X_1	$\phi(x; -1, 1.2)$	$[-4, 3]$
X_2	$\phi(x; 0.5, 0.7)$	$[-2, 4]$
X_3	$\phi(x; 1.6, 0.9)$	$[-3.5, 5]$
X_4	$\phi(x; -0.8, 1.5)$	$[-5, 2]$
X_5	$\phi(x; 0, 0.6)$	$[-2.5, 2.5]$

$$\text{Note: } \phi(x; m, s) = \frac{1}{\sqrt{2\pi}s} \exp\left(-\frac{(x-m)^2}{2s^2}\right).$$

**Figure 7:** Estimation of PoF using ITS: (a) $K = 4, r = 2$; and (b) $K = 8, r = 2$.

via ITS converges to the exact value as N_{ITS} increases. In particular, when $N_{\text{ITS}} > 4 \times 10^4$, the approximation error falls below 1%. For the second case, Fig. 7(b), computing the exact PoF would require 7,962,624 forward evaluations, which is infeasible given our computational resources. Instead, we compute a high-fidelity reference value of the PoF using a large number of samples, specifically $N_{\text{ITS}} = 2 \times 10^6$. The ITS estimate again exhibits convergence behavior. Once $N_{\text{ITS}} > 2 \times 10^4$, the variation in the estimated PoF is less than 1%. Based on these observations, we choose $N_{\text{ITS}} = 5 \times 10^4$ for all the computations in this and next examples and apply the selection criterion described in Section 2.4.6 and Algorithm 1. This implementation yields a reduction in computational cost by up to two orders of magnitude while maintaining acceptable accuracy.

Fig. 8 shows the best objective value at each generation during the DE iterations, together with the true PoF estimated via Monte Carlo sampling using 2×10^6 samples and the underlying truncated normal distributions. Remarkably, despite the discreteness, high dimensionality, and strong nonlinearity of the OUQ problem, all DE runs converge to stable optima within 200 generations. In particular, the objective values change by less than 1% over the final 100 iterations. This rapid convergence is largely attributable to the relatively large population size employed, set to 50 times the number of optimization variables in this example. Across all situations, the true PoF remains consistently bracketed by the optimal bounds throughout the iterations.

Fig. 9 compares the optimal bounds with the true PoF. The numerical values of the optimal bounds are summarized in Table 10 in Appendix C. As expected, increasing either the number of subdomains or the number of moment constraints decreases the upper bound U and increases the lower bound L , thereby tightening the bound interval. In the cases with the least uncertainty information—namely $K = 1, r = 0$; $K = 1, r = 1$; and $K = 2, r = 0$ —the optimal bounds are $[L, U] = [0, 1]$, which are uninformative. In contrast, in the case with the greatest amount of information, i.e., $K = 8, r = 2$, the optimal bounds are $[L, U] = [0.2925, 0.2988]$, deviating from the true PoF 0.2943 by only $[-0.61\%, +1.53\%]$.

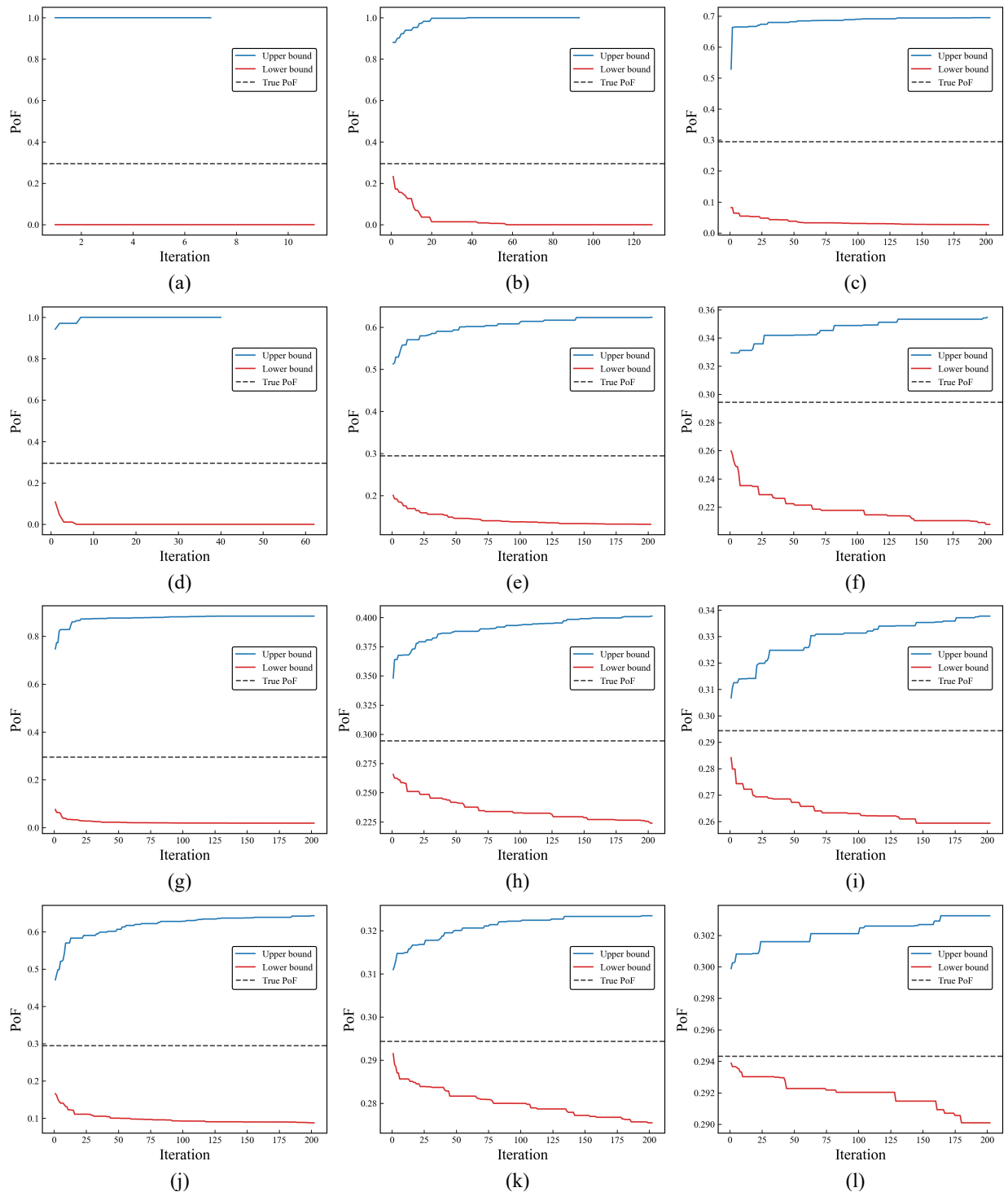


Figure 8: DE convergence under different situations: (a) $K = 1$, $r = 0$; (b) $K = 1$, $r = 1$; (c) $K = 1$, $r = 2$; (d) $K = 2$, $r = 0$; (e) $K = 2$, $r = 1$; (f) $K = 2$, $r = 2$; (g) $K = 4$, $r = 0$; (h) $K = 4$, $r = 1$; (i) $K = 4$, $r = 2$; (j) $K = 8$, $r = 0$; (k) $K = 8$, $r = 1$; and (l) $K = 8$, $r = 2$.

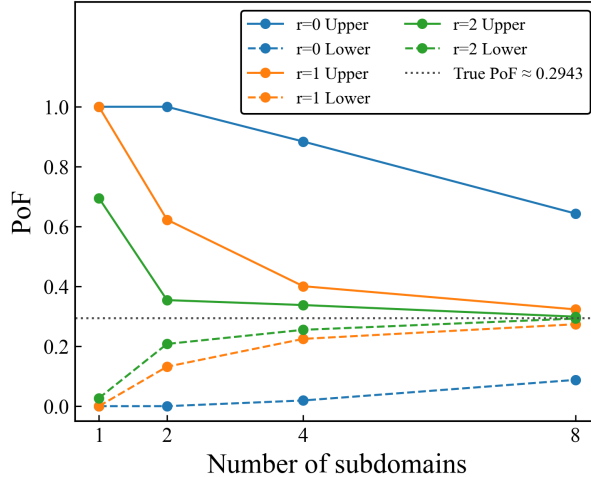


Figure 9: Optimal PoF bounds for the five-dimensional nonlinear problem.

Another notable observation from Fig. 9 is that both the upper and lower bounds are more sensitive to the number of moment constraints than to the number of subdomains. This conclusion can be drawn by comparing the optimal bounds for the cases $K = 4, r = 0$ and $K = 2, r = 1$. Since the dimension of the OUQ optimization problem is $mK(r + 1)$, both cases have the same computational cost in terms of evaluating the objective functions. However, the resulting bounds differ substantially. The bounds for $K = 2, r = 1$ are $[L, U] = [0.1319, 0.6229]$, which are significantly tighter than those for $K = 4, r = 0$, namely $[L, U] = [0.0190, 0.8839]$. A similar conclusion follows from comparing the cases $K = 8, r = 0$ and $K = 4, r = 1$. These findings suggest that, if the goal is to improve the tightness of the optimal bounds—and therefore the efficiency of certification—priority should be given to acquiring additional information in the form of higher-order local moment constraints rather than simply increasing the number of subdomains.

4.3. Case 3: A Ballistic Impact Problem

We next illustrate the developed OUQ framework through an application involving the performance of an AZ31B magnesium alloy plate subjected to normal impact by a heavy steel ball, as shown in Fig. 10(a). The plate measures 10 cm in both length and width, with a thickness of 0.35 cm, while the ball has a diameter of 1.12 cm. The impact velocity is 200 m/s. The design specification is defined in terms of the maximum backface deflection of the plate Y , illustrated in Fig. 10(b). The system is considered safe if the maximum backface deflection remains below a prescribed threshold Y_c . Otherwise, the design is deemed to have failed. Throughout this section, the failure threshold is set to $Y_c = 1.01$ cm. We further assume that all uncertainty arises from imperfect characterization of the constitutive response of the plate. As a representative scenario, the plate is assumed to be well described by the Johnson-Cook (JC) plasticity model [47] under the conditions of interest, while the model parameters remain uncertain. Partial information about the input probability measure is assumed to be available, specifically in the form of statistical moment constraints defined over subdomains. For simplicity, the projectile is assumed to be free of uncertainty.

4.3.1. Material Modeling

The constitutive behavior of the plate is described by a JC plasticity model [47], which is widely used to characterize the elastic-plastic response of ductile metals over broad ranges of strain rates and temperatures. Within this model, the flow stress is decomposed into contributions from strain hardening, strain-rate sensitivity, and thermal softening, and is expressed as

$$\sigma_y = [A + B \epsilon_{pl}^n] [1 + C \ln \dot{\epsilon}_{pl}^*] [1 - T^{*m}], \quad (36)$$

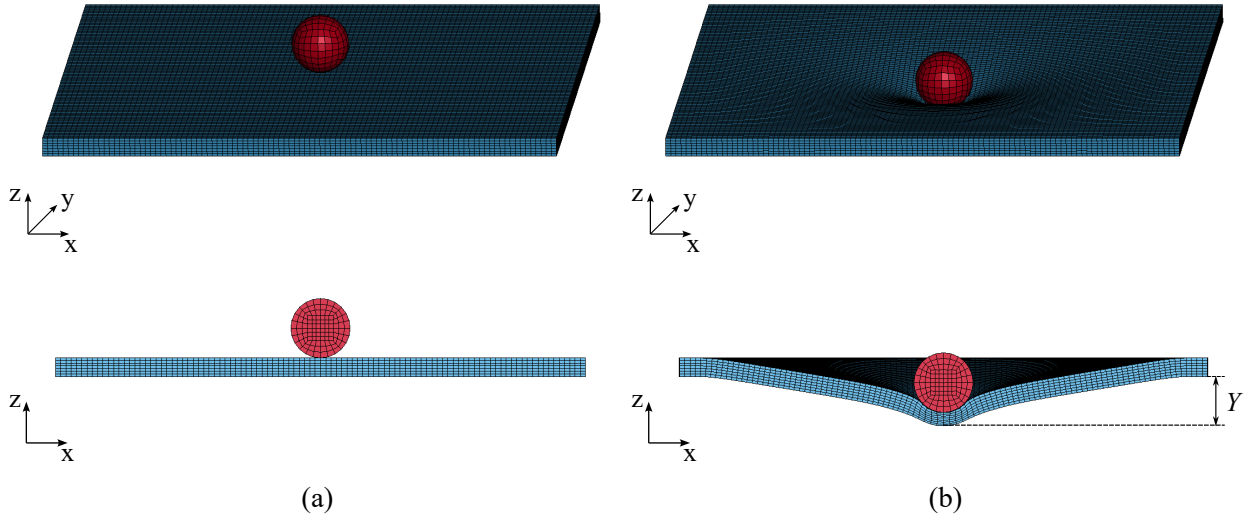


Figure 10: Schematic illustration of an AZ31B magnesium plate impacted by a spherical steel projectile at 200 m/s: (a) Initial configuration, and (b) Performance metric, with the maximum backface deflection denoted by Y . In each subfigure, the top figure shows a three-dimensional view of the projectile-plate system, while the bottom figure presents the corresponding mid-plane x - z cross-sectional view. Red and green markers denote the finite element models of the projectile and the plate, respectively.

where σ_y denotes the true flow stress and ϵ_{pl} is the equivalent plastic strain. The normalized plastic strain rate $\dot{\epsilon}_{pl}^*$ and the normalized temperature T^* are defined as

$$\dot{\epsilon}_{pl}^* = \frac{\dot{\epsilon}_{pl}}{\dot{\epsilon}_{pl0}}, \quad T^* = \frac{T - T_0}{T_m - T_0}, \quad (37)$$

where $\dot{\epsilon}_{pl}$ is the plastic strain rate, $\dot{\epsilon}_{pl0}$ is a reference plastic strain rate, T is the temperature, T_0 is the room temperature, and T_m is the melting temperature of the material. The random input vector is $X \equiv (A, B, n, C, m)$, where A denotes the quasi-static yield stress, B the hardening modulus, n the strain-hardening exponent, C the strain-rate sensitivity coefficient, and m the thermal softening exponent. These parameters are assumed to be mutually independent and uniformly distributed within prescribed bounds. The nominal values and bounds of these parameters are summarized in Table 3. Specifically, these values are obtained by fitting 10 stress-strain curves from quasi-static tensile tests, falling-weight impact tests, and tensile split Hopkinson bar tests, conducted over strain rates ranging from 0.003 to 1500 s⁻¹ and temperatures between 293 and 573 K [48]. The parameter bounds are determined using the 95% confidence intervals of the fitting results.

The volumetric response of the target plate is modeled using the Mie-Grüneisen equation of state [49]. The Taylor-Quinney factor is employed to quantify the fraction of plastic work converted into heat during plastic deformation [50]. Due to the substantial disparity in stiffness between AZ31B magnesium and steel, the projectile is assumed to behave as a rigid body. All remaining fixed material parameters for the target plate and the projectile are summarized in Tables 4 and 5, respectively.

4.3.2. Forward Solver and Surrogate Modeling

For a given realization of the material parameters, the maximum backface deflection Y is computed using an explicit finite-element solver implemented in LS-DYNA [54]. The projectile is discretized using 864 finite elements, while the plate is modeled with 70,000 elements. As shown in Fig. 10, all elements are linear hexahedral elements with single-point integration and appropriate hourglass control. The backface nodes of the target plate near the edges are fully constrained to prevent displacement in all directions. Normal contact between the projectile and the plate is enforced using a penalty-based contact formulation [54]. The time step is governed by the critical element size

Table 3

Nominal values and bounds of JC plasticity parameters determined by experiments [48].

Parameter	Nominal value	Lower bound	Upper bound	Unit
<i>A</i>	225.171	200.372	249.970	[MPa]
<i>B</i>	168.346	150.682	186.010	[MPa]
<i>n</i>	0.242	0.160	0.324	-
<i>C</i>	0.013	0.012	0.014	-
<i>m</i>	1.550	1.523	1.577	-

Table 4

Fixed material parameters for the AZ31B target plate.

Parameter	Value	Unit	Source
Mass density	1.77	[g/cm ³]	[48]
Young's Modulus	45.0	[GPa]	-
Poisson's ratio	0.35	-	-
Specific heat capacity	1.005	[J/(K·g)]	[51]
Taylor-Quinney factor	0.6	-	[52]
Reference strain rate	0.001	[s ⁻¹]	[48]
Reference Temperature	298.15	[K]	[48]
Reference melting Temperature	905.0	[K]	[48]
Grüneisen intercept	4520.0	[m/s]	[53]
Grüneisen gamma	1.54	-	[53]
Grüneisen slope	1.242	-	[53]

Table 5

Fixed material parameters for the steel projectile.

Parameter	Value	Unit
Mass density	7.83	[g/cm ³]
Young's Modulus	210.0	[GPa]
Poisson's ratio	0.30	-

according to the Courant-Friedrichs-Lowy (CFL) condition [55], and the total simulation time is set to 500 μ s, which is sufficient to capture the complete rebound of the projectile. All simulations are performed under adiabatic conditions, with the initial temperature set to room temperature.

Direct use of the LS-DYNA solver within the objective function of the OUQ optimization is computationally prohibitive. Therefore, we construct a data-driven neural-network surrogate \mathcal{N}_θ , parameterized by network parameters θ , to approximate the forward mapping from the JC parameter vector $X = (A, B, n, C, m)$ to the maximum backface deflection Y , i.e.,

$$Y = G(X) \approx \mathcal{N}_\theta(X). \quad (38)$$

A dataset of 5,400 samples is generated using the LS-DYNA solver with Latin hypercube sampling (LHS) over the input space defined in Table 3. The dataset is randomly partitioned into training, validation, and test sets with fixed proportions of 70%, 20%, and 10%, respectively [56]. The training set is used to fit the network parameters, the validation set is used for early stopping to prevent overfitting, and the test set is reserved for assessing the surrogate's generalization performance.

The surrogate model is implemented as a fully connected multilayer perceptron (MLP) with four hidden layers of 200 units each, yielding the architecture $5 \rightarrow 200 \rightarrow 200 \rightarrow 200 \rightarrow 200 \rightarrow 1$. Scaled exponential linear unit (SELU) activations [57] are employed in all hidden layers, with a linear activation at the output. The network is trained using the mean-squared error (MSE) loss and the Adam optimizer [58] with a learning rate of 10^{-3} , using mini-batches of size 32. Training is performed for up to 500 epochs with early stopping [59]. The validation MSE is monitored, and

training is terminated if no improvement is observed for 50 consecutive epochs. Model parameters are checkpointed whenever the validation loss reaches a new minimum, and the best-performing checkpoint is used for all subsequent evaluations.

The performance of the trained surrogate is summarized in Fig. 11. Fig. 11(a) shows the evolution of the training and validation MSE per epoch on a logarithmic y -axis, computed using only the training and validation datasets. The minimum validation MSE occurs at epoch 55, which is selected by the early-stopping criterion. The logarithmic scale highlights small-magnitude fluctuations while demonstrating that the validation loss remains low and stable around the selected checkpoint. Fig. 11(b) presents a parity plot evaluated exclusively on the test set, comparing predicted and true backface deflections (in cm). The data points closely follow the $y = x$ line without discernible bias, yielding a coefficient of determination (R^2) of 1.00, a root mean squared error (RMSE) of 1.57×10^{-4} cm, and a mean absolute error (MAE) of 1.25×10^{-4} cm. Because the test set is not used during training or model selection, this near-identity parity confirms that the surrogate generalizes well and is suitable for subsequent OUQ computations. These diagnostic results justify the use of $\mathcal{N}_\theta(X)$ as an accurate substitute for the LS-DYNA solver.

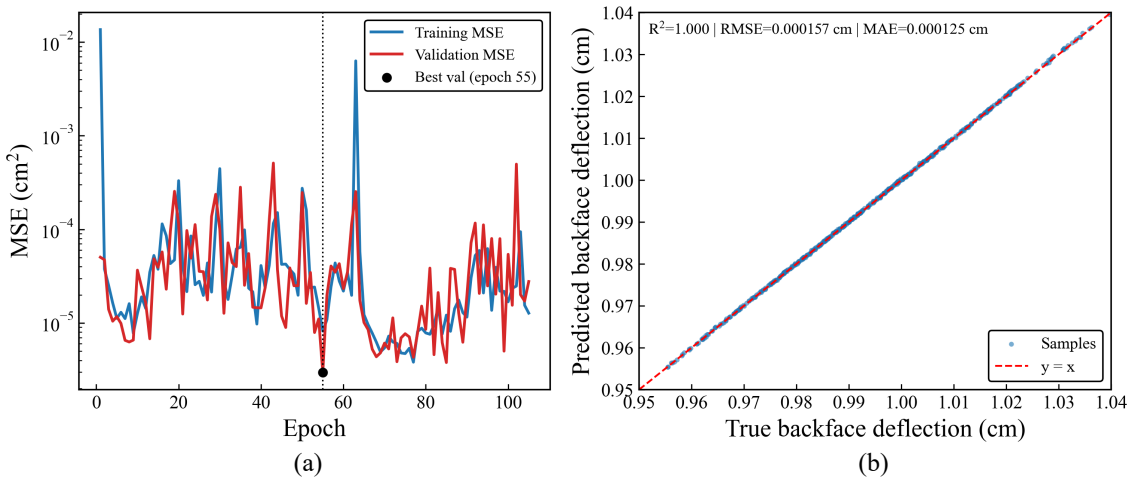


Figure 11: Surrogate model performance: (a) Training and validation MSE versus epoch on a logarithmic scale, and (b) Parity plot comparing predicted and true outputs on the test set.

To quantify the computational acceleration provided by the surrogate forward model, we benchmark its performance against the LS-DYNA solver on the same workstation using a single CPU core. A single LS-DYNA impact simulation requires approximately 333 s, whereas the surrogate model—evaluated conservatively in a batch size of one and averaged over 10^6 repeated calls to mitigate timing noise—achieves an average inference time of 8.435×10^{-5} s per sample. This corresponds to an approximate speedup of seven orders of magnitude. In practical OUQ or Monte Carlo calculations, model evaluations are typically executed in batches, which further improves computational throughput on a fixed hardware configuration. Consequently, the single-sample timing reported here represents a conservative lower bound on the achievable reduction in wall-clock time when deploying the surrogate model in large-scale UQ tasks.

4.3.3. OUQ Results Under Varying Levels of Uncertainty Information

We simultaneously partition the input domains of the five material parameters into $K = 1, 2, 4$, and 8 subdomains, and impose moment constraints up to second order, i.e., $r = 0, 1$, and 2. Fig. 12 compares the resulting optimal bounds with the true PoF, which is estimated via Monte Carlo sampling using the underlying truncated normal distributions. The numerical values of the optimal bounds are reported in Table 11 in Appendix C. Consistent with earlier examples, increasing either the number of subdomains or the number of moment constraints reduces the upper bound U and increases the lower bound L , thereby progressively tightening the OUQ interval. When the available uncertainty information is minimal—specifically in the case $K = 1, r = 0$ —the optimal bounds are $[L, U] = [0, 1]$, providing no useful certification information. In contrast, when the uncertainty description is most informative, namely for $K = 8$ and $r = 2$, the optimal bounds tighten to $[L, U] = [0.2101, 0.2480]$, deviating from the true PoF of 0.2297 by only $[-8.53\%, +7.97\%]$.

A further observation from Fig. 12 is that subdomain partitioning and moment constraints exhibit different efficiency-tightness trade-offs. When only subdomain information is imposed, the bounds can be tightened to $[L, U] = [0.1521, 0.3272]$ at $K = 8$, corresponding to deviations of $[-33.78\%, +42.46\%]$ from the true PoF. Conversely, when only moment constraints are imposed, the bounds tighten to $[L, U] = [0.0027, 0.5622]$ at $r = 2$, yielding much larger deviations of $[-98.83\%, +114.80\%]$. Although subdomain-only constraints produce tighter bounds than moment-only constraints, they also require higher computational cost.

Despite these differences, Fig. 12 also indicates that, for this ballistic impact problem, increasing the number of subdomains and increasing the order of moment constraints exert comparable influence on the overall tightness of the optimal bounds when computational cost is taken into account. For example, the bounds obtained for $K = 4$, $r = 0$, namely $[L, U] = [0.0625, 0.4375]$, are only slightly wider than those obtained for $K = 2$, $r = 1$, which yield $[L, U] = [0.1133, 0.4238]$. A similar pattern is observed when comparing the cases $K = 8$, $r = 0$ and $K = 4$, $r = 1$. These results suggest that, for this application, comparable improvements in PoF bound tightness can be achieved either by refining the subdomain partitioning or by enriching the uncertainty description through higher-order moment information across the material parameters.

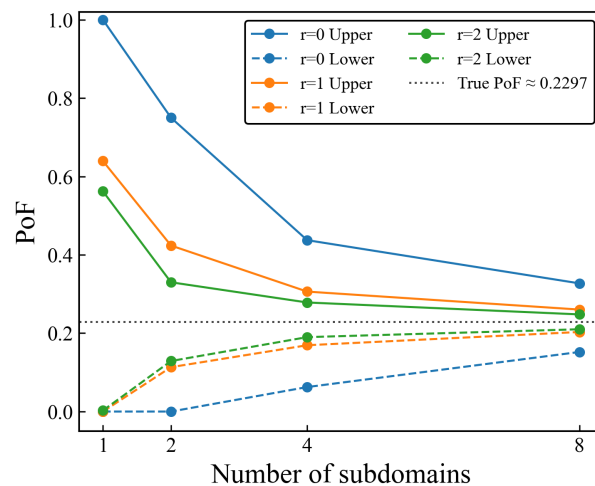


Figure 12: Optimal PoF bounds for the ballistic impact problem.

A previous study has shown that, when only the admissible ranges of the JC parameters (A, B, n, C, m) are specified, the maximum backface deflection Y is most sensitive to the quasi-static yield stress A [60]. That study quantified parameter sensitivity by computing McDiarmid's subdiameters, which measure the maximum change in system response induced by finite variations in individual input variables. Motivated by this finding, it is of interest to investigate how partial uncertainty information associated with A influences the resulting PoF bounds.

To this end, we conduct a one-dimensional OUQ analysis for the parameters A and B separately, while fixing the remaining JC parameters at their nominal values. The analysis for B serves as a point of comparison. For each parameter, we consider three cases— $K = 4$, $r = 0$; $K = 2$, $r = 1$; and $K = 1$, $r = 3$ —which entail identical computational cost in terms of objective function evaluations but differ in the type and amount of uncertainty information imposed. Fig. 13 reports the resulting optimal upper bounds U on the PoF. The corresponding lower bounds are uninformative in all cases and equal to zero.

The results show that, for parameter A , the optimal upper bound decreases markedly as the number of subdomains increases or, equivalently, as the moment constraints become less restrictive. This indicates that the PoF bound is more sensitive to subdomain partitioning than to higher-order moment information for the quasi-static yield stress. From a physical perspective, this suggests that improving the quasi-static strength of the target plate is an effective means of enhancing system safety. From a certification standpoint, however, tightening the PoF bounds and improving certification efficiency is better achieved by acquiring localized uncertainty information over subdomains rather than by refining global statistical moment constraints.

In contrast, for the hardening modulus B , the simultaneous imposition of subdomain partitioning and higher-order moment information—specifically in the case $K = 2, r = 1$ —yields the largest upper bound among the three scenarios considered. This behavior highlights the distinct roles that different material parameters play in uncertainty propagation and underscores the importance of tailoring uncertainty characterization strategies to parameter-specific sensitivities.

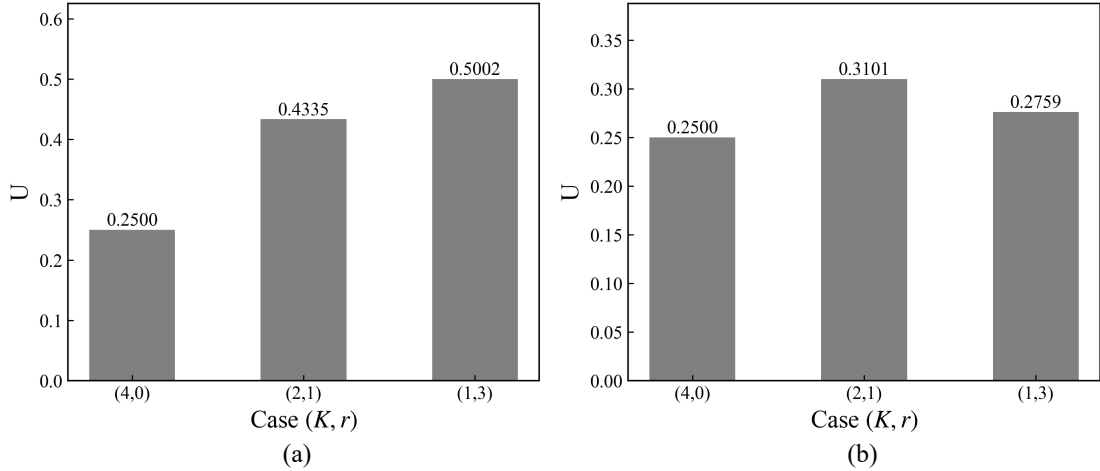


Figure 13: Optimal PoF upper bounds for one-dimensional OUQ analyses of the JC parameters: (a) quasi-static yield stress A , and (b) hardening modulus B , for three cases with identical computational cost.

5. Concluding Remarks

In this study, we have formulated an OUQ framework to account for uncertain inputs characterized by truncated moment constraints defined over input subdomains. We have developed a high-performance computational framework to compute rigorous optimal upper and lower bounds on the PoF over the admissible set of probability measures. The proposed methodology has integrated several key components: a reduction theory that transforms the original infinite-dimensional optimization problem over admissible probability measures into a finite-dimensional problem over admissible Dirac measures; the use of canonical moments that converts constrained optimization problems into unconstrained ones; eigendecomposition of the associated Jacobi matrix that mitigates ill-conditioning in root-finding procedures; and ITS that enables efficient and accurate evaluation of the PoF under Dirac measures.

We have presented three groups of numerical examples to evaluate the effectiveness of the proposed subdomain-based OUQ framework across varying numbers of subdomains and moment constraints. Based on these investigations, the following conclusions can be drawn:

1. The evidence theory can be regarded as a special case of the proposed OUQ methodology, in which the uncertain inputs are constrained only by zeroth-order moments over subdomains. In this setting, the plausibility and belief functions in the evidence theory correspond, respectively, to the optimal upper and lower bounds obtained from the OUQ.
2. For high-dimensional problems, the ITS strategy has reduced computational cost by up to two orders of magnitude while maintaining a relative error below 1%. By contrast, for low-dimensional problems, the cost of ITS may exceed that of directly evaluating the PoF using all Dirac combinations.
3. Across all numerical examples considered, a general trend is observed in which increasing either the number of subdomains or the order of moment constraints has systematically decreased the upper bound and increased the lower bound, thereby tightening the bound interval. In all cases, the true PoF is consistently bracketed by the corresponding optimal bounds.
4. We have identified regimes and input parameters for which the optimal bounds are more sensitive to subdomain partitioning or to higher-order moment information. These findings provide practical guidance for prioritizing uncertainty reduction efforts when certifying system safety.

5. For the ballistic impact problem, the PoF upper bound has been found to be more sensitive to subdomain partitioning than to higher-order moment information for quasi-static yield stress A , whereas no clear sensitivity trend is observed for the hardening modulus B .

In this work, we have focused on computing optimal PoF bounds for systems whose uncertain inputs are characterized by truncated moment constraints over input subdomains, a form of epistemic uncertainty. In many engineering applications, however, sufficient data may be available for certain uncertain quantities to justify probabilistic modeling using stochastic distributions, while only limited data exist for other quantities, precluding such representations. An important direction for future research is therefore the integration of aleatory uncertainties, described by stochastic distributions, with epistemic uncertainties characterized by moment constraints over subdomains, within a unified OUQ framework [24].

It is also worth noting that, in some instances, the upper or lower bounds remain unchanged despite the introduction of additional uncertainty information. This behavior arises when the added information pertains to regions of the input space that lie entirely within the safe and failure domain and therefore do not influence the bounds on PoF, which are primarily governed by probability mass near the boundary between the safe and failure domains. Consequently, uncertainty information provided on subdomains that intersect, but are not entirely contained within, the failure region is more effective for tightening the PoF bounds. These marginal subdomains may further benefit from finer partitioning or the incorporation of higher-order moment constraints to improve bound tightness more efficiently. Accordingly, the identification of failure regions in the input space and the development of adaptive subdomain partitioning strategies constitute promising directions for future research.

6. Acknowledgments

R.J. and X.S. gratefully acknowledge the support of the National Science Foundation (NSF), USA, under Grant No. 2429424, and the support of the University of Kentucky, USA, through the faculty start-up fund. The authors also thank Dr. Burigede Liu for generously sharing the learning-based OUQ codes.

Appendix

A. Optimal Bounds under Zeroth-Order Moment Constraints

As defined in Eq. (31), the failure domain \mathcal{X}^c is a subset of the input space \mathcal{X} . Using Eqs. (8) and (32), we obtain

$$\begin{aligned}
 \mathcal{X}^c &= \mathcal{X}^c \cap \mathcal{X} \\
 &= \left(\prod_{i=1}^m \mathcal{X}_i^c \right) \cap \left(\prod_{i=1}^m \bigcup_{j=1}^K \mathcal{X}_{i,j} \right) \\
 &= \prod_{i=1}^m \left(\mathcal{X}_i^c \cap \bigcup_{j=1}^K \mathcal{X}_{i,j} \right) \\
 &= \prod_{i=1}^m \bigcup_{j=1}^K \left(\mathcal{X}_i^c \cap \mathcal{X}_{i,j} \right).
 \end{aligned} \tag{39}$$

Substituting Eq. (39) into Eq. (30) and using the disjointness in Eq. (7), the PoF can be written as

$$\begin{aligned}
 \mu[Y \in \mathcal{Y}_c] &= \mu \left[X \in \prod_{i=1}^m \bigcup_{j=1}^K \left(\mathcal{X}_i^c \cap \mathcal{X}_{i,j} \right) \right] \\
 &= \bigotimes_{i=1}^m \mu_i \left[X_i \in \bigcup_{j=1}^K \left(\mathcal{X}_i^c \cap \mathcal{X}_{i,j} \right) \right] \\
 &= \bigotimes_{i=1}^m \sum_{j=1}^K \mu_i [X_i \in \mathcal{X}_i^c \cap \mathcal{X}_{i,j}].
 \end{aligned} \tag{40}$$

The last equality follows from the law of total probability.

Because the inputs are independent, the upper and lower bounds over the information set \mathcal{A} in Eq. (29) become

$$U(\mathcal{A}) = \prod_{i=1}^m \sup_{\mu \in \mathcal{A}} \sum_{j=1}^K \mu_i [X_i \in \mathcal{X}_i^c \cap \mathcal{X}_{i,j}], \quad (41a)$$

$$L(\mathcal{A}) = \prod_{i=1}^m \inf_{\mu \in \mathcal{A}} \sum_{j=1}^K \mu_i [X_i \in \mathcal{X}_i^c \cap \mathcal{X}_{i,j}]. \quad (41b)$$

In general, the supremum of a sum of functions does not equal the sum of their suprema, nor does the infimum distribute over summation. However, Proposition B.2 in Appendix B establishes that, for the particular structure of Eq. (41), the supremum and infimum do commute with the summation. Thus,

$$U(\mathcal{A}) = \prod_{i=1}^m \sum_{j=1}^K \sup_{\mu \in \mathcal{A}} \mu_i [X_i \in \mathcal{X}_i^c \cap \mathcal{X}_{i,j}], \quad (42a)$$

$$L(\mathcal{A}) = \prod_{i=1}^m \sum_{j=1}^K \inf_{\mu \in \mathcal{A}} \mu_i [X_i \in \mathcal{X}_i^c \cap \mathcal{X}_{i,j}]. \quad (42b)$$

Using Bayes' theorem and the known zeroth moments $M_{i,j,0}$ from Eq. (29), these bounds can be rewritten as

$$U(\mathcal{A}) = \prod_{i=1}^m \sum_{j=1}^K M_{i,j,0} \sup_{\mu \in \mathcal{A}} \mu_i [X_i \in \mathcal{X}_i^c \mid X_i \in \mathcal{X}_{i,j}], \quad (43a)$$

$$L(\mathcal{A}) = \prod_{i=1}^m \sum_{j=1}^K M_{i,j,0} \inf_{\mu \in \mathcal{A}} \mu_i [X_i \in \mathcal{X}_i^c \mid X_i \in \mathcal{X}_{i,j}]. \quad (43b)$$

Since only zeroth moments are specified, each conditional probability must satisfy

$$\mu_i [X_i \in \mathcal{X}_i^c \mid X_i \in \mathcal{X}_{i,j}] = \begin{cases} 0, & \mathcal{X}_i^c \cap \mathcal{X}_{i,j} = \emptyset, \\ 1, & \mathcal{X}_i^c \cap \mathcal{X}_{i,j} = \mathcal{X}_{i,j}, \\ \in (0, 1), & \text{otherwise.} \end{cases} \quad (44)$$

Thus, the extremal conditional probabilities are

$$\sup_{\mu \in \mathcal{A}} \mu_i [X_i \in \mathcal{X}_i^c \mid X_i \in \mathcal{X}_{i,j}] = \mathbf{1}[\mathcal{X}_i^c \cap \mathcal{X}_{i,j} \neq \emptyset], \quad (45a)$$

$$\inf_{\mu \in \mathcal{A}} \mu_i [X_i \in \mathcal{X}_i^c \mid X_i \in \mathcal{X}_{i,j}] = \mathbf{1}[\mathcal{X}_i^c \cap \mathcal{X}_{i,j} = \mathcal{X}_{i,j}]. \quad (45b)$$

Substituting these expressions into Eq. (42) yields the upper and lower bounds in Eq. (33).

B. Theorem and Proof

We begin by recalling a classical characterization of the supremum and infimum of a set of real numbers.

Theorem B.1 (Characterization of Supremum and Infimum). *Let $A \subset \mathbb{R}$, and suppose that both $\sup A$ and $\inf A$ exist. Then,*

1. $a = \sup A$ if and only if
 - (a) $y \leq a$ for all $y \in A$, and
 - (b) for every $\epsilon > 0$ there exists $x \in A$ such that $x > a - \epsilon$.
2. $a = \inf A$ if and only if
 - (a) $y \geq a$ for all $y \in A$, and
 - (b) for every $\epsilon > 0$ there exists $x \in A$ such that $x < a + \epsilon$.

Using Theorem B.1, we now establish a key proposition used in our derivation of the optimal bounds in Section A.

Proposition B.2. *Let \mathcal{X}_j ($j = 1, \dots, K$) be mutually disjoint subdomains of the sample space \mathcal{X} of the random variable X , and suppose $\mathcal{X}_j^* \subseteq \mathcal{X}_j$ for all j . Let \mathcal{A} be the set of all probability measures μ on \mathcal{X} satisfying the constraints*

$$\mathcal{A} = \{\mu : \mu[X \in \mathcal{X}_j] = M_j, j = 1, \dots, K\}.$$

Then,

$$\sup_{\mu \in \mathcal{A}} \sum_{j=1}^K \mu[X \in \mathcal{X}_j^*] = \sum_{j=1}^K \sup_{\mu \in \mathcal{A}} \mu[X \in \mathcal{X}_j^*], \quad (46)$$

$$\inf_{\mu \in \mathcal{A}} \sum_{j=1}^K \mu[X \in \mathcal{X}_j^*] = \sum_{j=1}^K \inf_{\mu \in \mathcal{A}} \mu[X \in \mathcal{X}_j^*]. \quad (47)$$

Proof. We prove the supremum identity. The infimum case is analogous.

For any $\mu \in \mathcal{A}$ and every j ,

$$\mu[X \in \mathcal{X}_j^*] \leq \sup_{\nu \in \mathcal{A}} \nu[X \in \mathcal{X}_j^*]. \quad (48)$$

Summing over j gives

$$\sum_{j=1}^K \mu[X \in \mathcal{X}_j^*] \leq \sum_{j=1}^K \sup_{\nu \in \mathcal{A}} \nu[X \in \mathcal{X}_j^*]. \quad (49)$$

Taking the supremum over $\mu \in \mathcal{A}$ yields

$$\sup_{\mu \in \mathcal{A}} \sum_{j=1}^K \mu[X \in \mathcal{X}_j^*] \leq \sum_{j=1}^K \sup_{\nu \in \mathcal{A}} \nu[X \in \mathcal{X}_j^*]. \quad (50)$$

For each fixed j , define the constraint set

$$\mathcal{A}_j := \{\mu : \mu[X \in \mathcal{X}_j] = M_j\},$$

i.e., the local constraint on the subdomain \mathcal{X}_j . Since \mathcal{X}_j 's are disjoint and \mathcal{A} imposes these constraints independently, we have

$$\sup_{\mu \in \mathcal{A}} \mu[X \in \mathcal{X}_j^*] = \sup_{\mu \in \mathcal{A}_j} \mu[X \in \mathcal{X}_j^*]. \quad (51)$$

By the characterization of supremum (Theorem B.1), for any $\epsilon > 0$ there exists a measure $\mu_j^\epsilon \in \mathcal{A}_j$ such that

$$\mu_j^\epsilon[X \in \mathcal{X}_j^*] > \sup_{\nu \in \mathcal{A}_j} \nu[X \in \mathcal{X}_j^*] - \frac{\epsilon}{K}. \quad (52)$$

Now define a new probability measure μ^ϵ on \mathcal{X} by

$$\mu^\epsilon[X \in \mathcal{B}] = \sum_{j=1}^K \mu_j^\epsilon[X \in \mathcal{B} \cap \mathcal{X}_j], \quad \mathcal{B} \subseteq \mathcal{X}. \quad (53)$$

Since the \mathcal{X}_j 's are disjoint and $\mu_j^\epsilon(\mathcal{X}_j) = M_j$, this measure satisfies all constraints and thus

$$\mu^\epsilon \in \mathcal{A}. \quad (54)$$

Then,

$$\mu^\epsilon[X \in \mathcal{X}_j^*] = \mu_j^\epsilon[X \in \mathcal{X}_j^*], \quad (55)$$

and summing over j , using (52),

$$\sum_{j=1}^K \mu^\epsilon[X \in \mathcal{X}_j^*] > \sum_{j=1}^K \left(\sup_{\nu \in \mathcal{A}_j} \nu[X \in \mathcal{X}_j^*] - \frac{\epsilon}{K} \right) = \sum_{j=1}^K \sup_{\nu \in \mathcal{A}} \nu[X \in \mathcal{X}_j^*] - \epsilon. \quad (56)$$

Because $\epsilon > 0$ is arbitrary and $\mu^\epsilon \in \mathcal{A}$,

$$\sup_{\mu \in \mathcal{A}} \sum_{j=1}^K \mu[X \in \mathcal{X}_j^*] \geq \sum_{j=1}^K \sup_{\nu \in \mathcal{A}} \nu[X \in \mathcal{X}_j^*]. \quad (57)$$

From (50) and (57), equality follows

$$\sup_{\mu \in \mathcal{A}} \sum_{j=1}^K \mu[X \in \mathcal{X}_j^*] = \sum_{j=1}^K \sup_{\nu \in \mathcal{A}} \nu[X \in \mathcal{X}_j^*].$$

A parallel argument proves the infimum identity. This completes the proof. \square

C. Numerical Values of Optimal Bounds and Relative Deviations

This section reports the numerical values of the optimal bounds via OUQ together with their relative deviations. Results are provided for the one-dimensional examples in Tables 6-9 (Section 4.1), the five-dimensional nonlinear problem in Table 10 (Section 4.2), and the ballistic impact problem in Table 11 (Section 4.3).

References

- [1] N. Kovachki, B. Liu, X. Sun, H. Zhou, K. Bhattacharya, M. Ortiz, A. Stuart, Multiscale modeling of materials: Computing, data science, uncertainty and goal-oriented optimization, *Mechanics of Materials* 165 (2022) 104156.
- [2] B. Liu, X. Sun, K. Bhattacharya, M. Ortiz, Hierarchical multiscale quantification of material uncertainty, *Journal of the Mechanics and Physics of Solids* 153 (2021) 104492.
- [3] R. Jin, G. Wang, X. Sun, Ensemble-based data assimilation for material model characterization in high-velocity impact, *arXiv preprint arXiv:2510.09703* (2025).
- [4] A. Der Kiureghian, O. Ditlevsen, Aleatory or epistemic? does it matter?, *Structural safety* 31 (2009) 105–112.
- [5] W. K. Hastings, Monte carlo sampling methods using markov chains and their applications (1970).
- [6] A. P. Dempster, A generalization of bayesian inference, *Journal of the Royal Statistical Society: Series B (Methodological)* 30 (1968) 205–232.
- [7] T. Fetz, M. Oberguggenberger, Propagation of uncertainty through multivariate functions in the framework of sets of probability measures, *Reliability Engineering & System Safety* 85 (2004) 73–87.
- [8] J. Zhang, M. D. Shields, The effect of prior probabilities on quantification and propagation of imprecise probabilities resulting from small datasets, *Computer Methods in Applied Mechanics and Engineering* 334 (2018) 483–506.

Table 6

Optimal bounds and relative deviations for the one-dimensional truncated normal case.

r	K	U	RD of U (%)	L	RD of L (%)
0	1	1.0000	+313.22	0.0000	-100.00
	2	0.5000	+106.61	0.0000	-100.00
	4	0.5000	+106.61	0.0062	-97.36
	8	0.5000	+106.61	0.1056	-56.36
1	1	0.8772	+262.48	0.0000	-100.00
	2	0.5000	+106.61	0.0114	-95.37
	4	0.5000	+106.61	0.0261	-89.21
	8	0.4146	+71.24	0.1056	-56.36
2	1	0.6711	+177.36	0.0000	-100.00
	2	0.5000	+106.61	0.0128	-94.71
	4	0.4465	+84.55	0.0469	-80.62
	8	0.3979	+64.42	0.1269	-47.56
3	1	0.6349	+162.36	0.0042	-98.26
	2	0.4145	+71.20	0.0819	-66.16
	4	0.4097	+69.30	0.0924	-61.82
	8	0.3556	+46.94	0.1436	-40.66

Note: RD denotes relative deviation, computed with respect to the true PoF of 0.2420.

Table 7

Optimal bounds and relative deviations for the one-dimensional uniform case.

r	K	U	RD of U (%)	L	RD of L (%)
0	1	1.0000	+203.03	0.0000	-100.00
	2	0.5000	+51.52	0.0000	-100.00
	4	0.5000	+51.52	0.2500	-24.24
	8	0.3750	+13.64	0.2500	-24.24
1	1	0.7463	+126.15	0.0000	-100.00
	2	0.5000	+51.52	0.1212	-63.27
	4	0.4338	+31.45	0.2500	-24.24
	8	0.3750	+13.64	0.2773	-15.97
2	1	0.7425	+125.00	0.0000	-100.00
	2	0.4951	+50.03	0.1237	-62.52
	4	0.4300	+30.30	0.2500	-24.24
	8	0.3704	+12.24	0.2799	-15.18
3	1	0.5966	+80.79	0.0982	-70.24
	2	0.4482	+35.82	0.1965	-40.45
	4	0.3966	+20.18	0.2731	-17.24
	8	0.3608	+9.33	0.2963	-10.21

Note: RD denotes relative deviation, computed with respect to the true PoF of 0.3300.

- [9] J. Zhang, M. D. Shields, On the quantification and efficient propagation of imprecise probabilities resulting from small datasets, *Mechanical Systems and Signal Processing* 98 (2018) 465–483.
- [10] A. P. Dempster, Upper and lower probabilities induced by a multivalued mapping, in: *Classic works of the Dempster-Shafer theory of belief functions*, Springer, 2008, pp. 57–72.
- [11] G. Shafer, *A mathematical theory of evidence* (2020).
- [12] S. Ferson, J. G. Hajagos, Arithmetic with uncertain numbers: rigorous and (often) best possible answers, *Reliability Engineering & System Safety* 85 (2004) 135–152.
- [13] K. Weichselberger, The theory of interval-probability as a unifying concept for uncertainty, *International Journal of Approximate Reasoning* 24 (2000) 149–170.

Table 8

Optimal bounds and relative deviations for the one-dimensional truncated Weibull case.

r	K	U	RD of U (%)	L	RD of L (%)
0	1	1.0000	+527.53	0.0000	-100.00
	2	1.0000	+527.53	0.0192	-87.94
	4	0.2472	+55.18	0.0192	-87.94
	8	0.2472	+55.18	0.0767	-51.86
1	1	0.6018	+277.78	0.0000	-100.00
	2	0.5840	+266.61	0.0192	-87.94
	4	0.2472	+55.18	0.0574	-63.98
	8	0.2472	+55.18	0.0828	-48.02
2	1	0.5127	+221.84	0.0000	-100.00
	2	0.4376	+174.70	0.0192	-87.94
	4	0.2472	+55.18	0.0688	-56.82
	8	0.2189	+37.44	0.1017	-36.15
3	1	0.4632	+190.78	0.0034	-97.87
	2	0.3979	+149.81	0.0339	-78.73
	4	0.2262	+41.97	0.0863	-45.81
	8	0.2148	+34.87	0.1098	-31.05

Note: RD denotes relative deviation, computed with respect to the true PoF of 0.1593.

Table 9

Optimal bounds and relative deviations for the one-dimensional truncated bimodal normal-mixture case.

r	K	U	RD of U (%)	L	RD of L (%)
0	1	1.0000	+102.96	0.0000	-100.00
	2	0.6432	+30.55	0.0000	-100.00
	4	0.6432	+30.55	0.1999	-59.44
	8	0.5027	+2.03	0.1999	-59.44
1	1	0.8887	+80.36	0.0000	-100.00
	2	0.6432	+30.55	0.1269	-74.27
	4	0.6432	+30.55	0.2860	-41.96
	8	0.5027	+2.03	0.3488	-29.21
2	1	0.8778	+78.17	0.0185	-96.27
	2	0.6432	+30.55	0.2395	-51.40
	4	0.6198	+25.80	0.3113	-36.82
	8	0.5027	+2.03	0.4235	-14.05
3	1	0.7781	+57.94	0.0698	-85.86
	2	0.6281	+27.49	0.2673	-45.76
	4	0.6112	+24.06	0.3437	-30.25
	8	0.5027	+2.03	0.4467	-9.34

Note: RD denotes relative deviation, computed with respect to the true PoF of 0.4927.

- [14] J. J. Buckley, Fuzzy probabilities: new approach and applications, Springer, 2005.
- [15] M. Beer, S. Ferson, V. Kreinovich, Imprecise probabilities in engineering analyses, Mechanical systems and signal processing 37 (2013) 4–29.
- [16] M. Götz, W. Graf, M. Kaliske, Structural design with polymorphic uncertainty models, International Journal of Reliability and Safety 9 (2015) 112–131.
- [17] H. Owhadi, C. Scovel, T. J. Sullivan, M. McKerns, M. Ortiz, Optimal uncertainty quantification, Siam Review 55 (2013) 271–345.
- [18] G. Winkler, et al., Integral representation in the set of solutions of a generalized moment problem, Mathematische Annalen 246 (1979) 23–32.
- [19] G. Winkler, Extreme points of moment sets, Mathematics of Operations Research 13 (1988) 581–587.

Table 10

Optimal bounds and relative deviations for the five-dimensional nonlinear problem.

r	K	U	RD of U (%)	L	RD of L (%)
0	1	1.0000	+239.70	0.0000	-100.00
	2	1.0000	+239.70	0.0000	-100.00
	4	0.8839	+200.30	0.0190	-93.57
	8	0.6433	+118.60	0.0878	-70.20
1	1	1.0000	+239.70	0.0000	-100.00
	2	0.6229	+111.60	0.1319	-55.20
	4	0.4007	+36.16	0.2247	-23.65
	8	0.3232	+9.82	0.2736	-7.03
2	1	0.6949	+136.10	0.0269	-90.84
	2	0.3542	+20.36	0.2078	-29.39
	4	0.3377	+14.75	0.2550	-13.36
	8	0.2988	+1.53	0.2925	-0.61

Note: RD denotes relative deviation, computed with respect to the true PoF of 0.2943.

Table 11

Optimal bounds and relative deviations for the ballistic impact problem.

r	K	U	RD of U (%)	L	RD of L (%)
0	1	1.0000	+335.40	0.0000	-100.00
	2	0.7500	+226.60	0.0000	-100.00
	4	0.4375	+90.45	0.0625	-72.80
	8	0.3272	+42.46	0.1521	-33.78
1	1	0.6395	+178.40	0.0000	-100.00
	2	0.4238	+84.50	0.1133	-50.70
	4	0.3062	+33.32	0.1693	-26.30
	8	0.2603	+13.33	0.2031	-11.58
2	1	0.5622	+144.80	0.0027	-98.83
	2	0.3300	+43.66	0.1290	-43.83
	4	0.2784	+21.21	0.1900	-17.29
	8	0.2480	+7.97	0.2101	-8.53

Note: RD denotes relative deviation, computed with respect to the true PoF of 0.2297.

- [20] J. Stenger, Optimal uncertainty quantification of a risk measurement from a computer code, Ph.D. thesis, Université Paul Sabatier-Toulouse III, 2020.
- [21] P.-H. Kamga, B. Li, M. McKerns, L. Nguyen, M. Ortiz, H. Owhadi, T. Sullivan, Optimal uncertainty quantification with model uncertainty and legacy data, *Journal of the Mechanics and Physics of Solids* 72 (2014) 1–19.
- [22] X. Sun, Uncertainty quantification of material properties in ballistic impact of magnesium alloys, *Materials* 15 (2022) 6961.
- [23] D. Balzani, T. Schmidt, M. Ortiz, Method for the quantification of rupture probability in soft collagenous tissues, *International journal for numerical methods in biomedical engineering* 33 (2017) e02781.
- [24] N. Miska, D. Balzani, Method for the analysis of epistemic and aleatory uncertainties for a reliable evaluation of failure of engineering structures, *International Journal for Uncertainty Quantification* 12 (2022).
- [25] N. Miska, D. Balzani, Reliability-based design optimization incorporating extended optimal uncertainty quantification, *Probabilistic Engineering Mechanics* 80 (2025) 103755.
- [26] J. Stenger, F. Gamboa, M. Keller, Optimization of quasi-convex function over product measure sets, *SIAM Journal on Optimization* 31 (2021) 425–447.
- [27] D. Wang, H. Qiu, L. Gao, C. Jiang, A subdomain uncertainty-guided kriging method with optimized feasibility metric for time-dependent reliability analysis, *Reliability Engineering & System Safety* 243 (2024) 109839.
- [28] Y. Zhao, J. Yang, M. G. Faes, S. Bi, Y. Wang, The sub-interval similarity: A general uncertainty quantification metric for both stochastic and interval model updating, *Mechanical Systems and Signal Processing* 178 (2022) 109319.
- [29] J. Liu, X. Sun, K. Li, C. Jiang, X. Han, A probability density function discretization and approximation method for the dynamic load identification of stochastic structures, *Journal of Sound and Vibration* 357 (2015) 74–94.

[30] C. Jiang, X. Han, G. Liu, Optimization of structures with uncertain constraints based on convex model and satisfaction degree of interval, *Computer Methods in Applied Mechanics and Engineering* 196 (2007) 4791–4800.

[31] X. Yin, W. Chen, A. To, C. McVeigh, W. K. Liu, Statistical volume element method for predicting microstructure–constitutive property relations, *Computer methods in applied mechanics and engineering* 197 (2008) 3516–3529.

[32] R. Ahlfeld, B. Belkouchi, F. Montomoli, Samba: Sparse approximation of moment-based arbitrary polynomial chaos, *Journal of Computational Physics* 320 (2016) 1–16.

[33] K. Sepahvand, S. Marburg, Identification of composite uncertain material parameters from experimental modal data, *Probabilistic Engineering Mechanics* 37 (2014) 148–153.

[34] J. Stenger, F. Gamboa, M. Keller, B. Iooss, Optimal uncertainty quantification of a risk measurement from a thermal-hydraulic code using canonical moments, *International Journal for Uncertainty Quantification* 10 (2020).

[35] M. McKerns, H. Owhadi, C. Scovel, T. J. Sullivan, M. Ortiz, The optimal uncertainty algorithm in the mystic framework, *arXiv preprint arXiv:1202.1055* (2012).

[36] R. Storn, K. Price, Differential evolution—a simple and efficient heuristic for global optimization over continuous spaces, *Journal of global optimization* 11 (1997) 341–359.

[37] X. Sun, B. Liu, A learning-based optimal uncertainty quantification method and its application to ballistic impact problems, *Mechanics of Materials* 184 (2023) 104727.

[38] H. Dette, W. J. Studden, *The theory of canonical moments with applications in statistics, probability, and analysis*, John Wiley & Sons, 1997.

[39] P. Henrici, *Applied and computational complex analysis, Volume 3: Discrete Fourier analysis, Cauchy integrals, construction of conformal maps, univalent functions*, volume 3, John Wiley & Sons, 1993.

[40] W. Gautschi, *Orthogonal polynomials: computation and approximation*, OUP Oxford, 2004.

[41] G. H. Golub, J. H. Welsch, Calculation of gauss quadrature rules, *Mathematics of computation* 23 (1969) 221–230.

[42] C. P. Robert, G. Casella, G. Casella, *Monte Carlo statistical methods*, volume 2, Springer, 1999.

[43] R. Y. Rubinstein, D. P. Kroese, *Simulation and the Monte Carlo method*, John Wiley & Sons, 2016.

[44] Q.-M. Carlo, *Monte carlo methods in financial engineering*, 2001.

[45] M. Rossetti, Simulation modeling using the kotlin simulation library (ksl), under the Creative Commons Attribution-Noncommercial-No Derivatives 4.0 International License (2023).

[46] K. V. Price, R. M. Storn, J. A. Lampinen, *Differential evolution: a practical approach to global optimization*, Springer, 2005.

[47] G. R. Johnson, A constitutive model and data for materials subjected to large strains, high strain rates, and high temperatures, *Proc. 7th Inf. Sympo. Ballistics* (1983) 541–547.

[48] D. Hasenpouth, Tensile high strain rate behavior of AZ31B magnesium alloy sheet, Master's thesis, University of Waterloo, 2010.

[49] E. Grüneisen, Theorie des festen zustandes einatomiger elemente, *Annalen der Physik* 344 (1912) 257–306.

[50] G. I. Taylor, H. Quinney, The latent energy remaining in a metal after cold working, *Proceedings of the Royal Society of London. Series A, Containing Papers of a Mathematical and Physical Character* 143 (1934) 307–326.

[51] S. Lee, H. J. Ham, S. Y. Kwon, S. W. Kim, C. M. Suh, Thermal conductivity of magnesium alloys in the temperature range from- 125 c to 400 c, *International Journal of Thermophysics* 34 (2013) 2343–2350.

[52] O. T. Kingstedt, J. T. Lloyd, On the conversion of plastic work to heat in mg alloy az31b for dislocation slip and twinning deformation, *Mechanics of Materials* 134 (2019) 176–184.

[53] J. Feng, P. Chen, Q. Zhou, K. Dai, E. An, Y. Yuan, Numerical simulation of explosive welding using smoothed particle hydrodynamics method, *The International Journal of Multiphysics* 11 (2017) 315–326.

[54] LS-DYNA Theory Manual, Livermore Software Technology, ANSYS Company, Livermore, California, 2024. URL: https://ftp.lstc.com/anonymous/outgoing/web/ls-dyna_manuals/DRAFT/DRAFT_Theory.pdf.

[55] R. Courant, K. Friedrichs, H. Lewy, Über die partiellen differenzengleichungen der mathematischen physik, *Mathematische annalen* 100 (1928) 32–74.

[56] C. M. Bishop, N. M. Nasrabadi, *Pattern recognition and machine learning*, volume 4, Springer, 2006.

[57] G. Klambauer, T. Unterthiner, A. Mayr, S. Hochreiter, Self-normalizing neural networks, *Advances in neural information processing systems* 30 (2017).

[58] D. P. Kingma, Adam: A method for stochastic optimization, *arXiv preprint arXiv:1412.6980* (2014).

[59] L. Prechelt, Early stopping-but when?, in: *Neural Networks: Tricks of the trade*, Springer, 2002, pp. 55–69.

[60] X. Sun, T. Kirchdoerfer, M. Ortiz, Rigorous uncertainty quantification and design with uncertain material models, *International Journal of Impact Engineering* 136 (2020) 103418.